DARK CURRENT CONTROL IN InAs/GaSb SUPERLATTICE PHOTODETECTORS

A THESIS
SUBMITTED TO THE DEPARTMENT OF PHYSICS
AND THE GRADUATE SCHOOL OF ENGINEERING AND SCIENCE
OF BILKENT UNIVERSITY
IN PARTIAL FULFILLMENT OF THE REQUIREMENTS
FOR THE DEGREE OF
MASTER OF SCIENCE

By
Abdullah Muti
January, 2013

I certify that I have read this thesis and that in my opinion it is fully adequate, in scope and in quality, as a thesis for the degree of Master of Science.

_____.
Prof. Dr. Atilla Aydınlı

I certify that I have read this thesis and that in my opinion it is fully adequate, in scope and in quality, as a thesis for the degree of Master of Science.

_____.
Prof. Dr. Raşit Turan

I certify that I have read this thesis and that in my opinion it is fully adequate, in scope and in quality, as a thesis for the degree of Master of Science.

_____.
Assoc. Prof. Dr. Ceyhun Bulutay

Approved for the Graduate School of Engineering and Science:

_____.
Prof. Dr. Levent Onural
Director of the Graduate School

ABSTRACT
DARK CURRENT CONTROL IN InAs/GaSb SUPERLATTICE PHOTODETECTORS

Abdullah Muti

M.S. in Physics

Supervisor: Prof. Dr. Atilla Aydınlı

January,2013

Since every object with a finite temperature accepted to emit infrared radiation, detection of this part of the electromagnetic spectrum is very important. For example the temperature of the exhaust of a vehicle or a missile makes it radiate in the mid-wave window or the body temperature of a person makes it glow in the long-wave window. Therefore detection in mid-wave and long-wave windows of infrared radiation spectrum is useful for both military and civil purposes. In order to satisfy the need in these field thermal and optical detectors are being developed. Optical detectors are based on the absorption of the thermally generated photons from the objects. However, due to the low energy of the infrared radiation narrow band gap materials are needed to be used. Having narrow gap seems to be useful but the energy required to make an electron to excite from the valance band to conduction band can also be supplied by the ambient temperature. This situation is the main disadvantage of optical detectors. There are too many mechanisms that can generate dark current in the device which make the optically generated current to be less measurable and reduce the device performance. In order to solve this unintentional current problem, optical detectors should be cooled down to cryogenic temperatures. Even for this low temperature regime generation-recombination, tunneling and surface leak currents are not suppressed enough. To increase the device performance these mechanisms should be suppressed. Suppression of surface leakage current which is caused by the dangling bonds on the device side-walls can be achieved with a passivation layer that eliminates the surface states. This thesis suggests the usage of two new methods for passivation of InAs/GaSb type II superlattice mid-wave infrared detectors. Application of atomic layer deposited Al_2O_3 and monolayer thick octadecanethiol as passivation layers are compared with their respective unpassivated detectors on their effect on suppression of dark current. Additionally, contact resistance measurements are made in order to check that if there is a contribution from the contact structures that can complicate our device model.

Keywords: InAs/GaSb, Infrared photodetector, Passivation, Al_2O_3, Octadecanethiol

ÖZET
InAs/GaSb SÜPERÖRGÜ FOTODEDEKTÖRLERDE KARANLIK AKIM KONTROLÜ

Abdullah Muti

Fizik, Yüksek Lisans

Tez Yöneticisi: Prof. Dr. Atilla Aydınlı

Ocak, 2013

Belirli bir sıcaklığı olan bütün cisimlerin kızılötesi radyasyon yayması sebebiyle elektromanyetik spektrumun bu bölümünün dedekte edilmesi çok önemlidir. Örneğin bir aracın ya da bir füzenin eksozunun sıcaklığı orta dalgaboyunda ışıma, ya da bir insanın vücut sıcaklığı uzun dalgaboyunda ışıma sağlar. Bu yüzden kızılötesi ışıma spektrumunun orta ve uzun dalgaboyu pencerelerinin dedekte edilmesi askeri ve sivil amaçlar için yaralıdır. Bu alandaki ihtiyacı karşılamak için termal ve optic dedektörler geliştirilmektedir. Optik dedektörler cisimlerden termal olarak yayılan fotonların soğurulmasına dayanır. Fakat kızılötesi radyasyonun düşük enerjileri sebebiyle dar bant aralığına sahip malzemelere ihtiyaç duyulmaktadır. Dar bant aralığı faydalı görülse de bir elektronun değerlik bandından iletim bandına uyarılması için gereken enerji ortam sıcaklığı tarafından da sağlanabilir. Bu durum optik dedektörlerin temel sorunudur. Optik olarak oluşturulan akımın daha az ölçülebilir olmasına sebep verebilen ve alet perfomansını düşürebilen pek çok karanlık akım mekanizması bulunmaktadır. Bu istenmeyen akım problemini çözebilmek için optik dedektörler düşük sıcaklıklara soğutulması gerekir. Bu çok düşük sıcaklık bölgelerinde bile üretme-tüketme, tünelleme ve yüzey kaçak akımları yeterince baskılanamamaktadır. Alet performansının arttırılması için bu akımların baskılanması gerekmektedir. Alet yan yüzeylerindeki boş bağların sebep olduğu yüzey kaçak akımının baskılanması bu bağları etkisizleştirecek bir pasivasyon tabakasıyla sağlanabilir. Bu tez InAs/GaSb tip II süperörgü orta dalgaboyu kızılötesi dedektörleri için iki yeni pasivasyon yöntemi önermektedir. Atomik katman biriktirme yöntemiyle oluşturulmuş Al_2O_3 ve tek katman kalınlığında kaplanmış octadecanethiol pasivasyonları, pasivasyon uygulanmamış örneklerle karanlık akım baskılamaları yönünden karşılaştırılmıştır. Ayrıca alet modelini karmaşıklaştıracak katkıların olup olmadığını kontrol etmek için kontak direnci ölçümleri yapılmıştır.

Anahtar kelimeler; InAs/GaSb, kızılötesi fotodedektör, pasivasyon, Al_2O_3, octadecanethiol

Acknowledgement

I would like to express my gratitude to my supervisor Prof. Dr. Atilla Aydınlı for his limitless encouragement, guidance and patience during my research.

I am grateful to Dr. Ömer Salihoğlu for sharing his wisdom and teaching me the cleanroom processes.

I would like to thank to Prof. Dr. Raşit Turan for letting me use the optical measurements setup in METU and also for being in my thesis committee, reading and commenting on my thesis.

I would like to thank to Assoc. Prof. Dr. Ceyhun Bulutay for being in my thesis committee and for reading and commenting on my thesis.

I would like to thank to Dr. Tunay Tansel and Kutlu Kutluer for helping me in my optical measurements.

I would like to thank to Ertuğrul Karademir, Osman Balcı and Gonca Aras for sharing their knowledge on cleanroom with me.

I would like to thank to Özge Akay, Simge Ateş, Sinan Gündoğdu, Melike Gümüş, Nurbek Kakenov and Seval Sarıtaş for their friendship and support.

I would like to thank to Murat Güre and Ergün Karaman for keeping our labs running.

Finally, I would like to thank to my family for their endless support and love.

Contents

List of Figures

List of tables

Chapter 1

Introduction

In this chapter I present basic knowledge about infrared spectrum and its detection. Detection mechanisms, methods will be described. The working principles of photon detectors will be summarized. Some of the main photon detector technologies will be explained briefly. As the infrared detection technology used for this thesis, superlattice structures will be introduced in more detail. Fabrication technology and in particular, the requirements for passivation will be summarized.

1.1 Infrared Radiation

Infrared radiation originates from the thermally emitted photons from any object that has temperature above 0 Kelvin. It might be said that infrared radiation is electromagnetic radiation caused by temperature of an object. Due to the fact that every object has a finite temperature, detection of infrared radiation is often necessary and useful. For different temperatures wavelength of the radiation shows different distribution of intensity and different peak intensity values. At room temperature (~300 K) we don't see the objects glow in the dark, because most of the emitted light is not in the visible range. However, molten iron glows in the visible range due to temperatures of 1500 K or more. The sun which has a temperature of ~5000 K emits light which has more photons in the visible range than molten iron. The relations between the temperature of the object and the wavelength distribution of the emitted radiation are described by Planck's law, Wien's law and Stefan-Boltzmann law which are based on the idealized concept of blackbody.

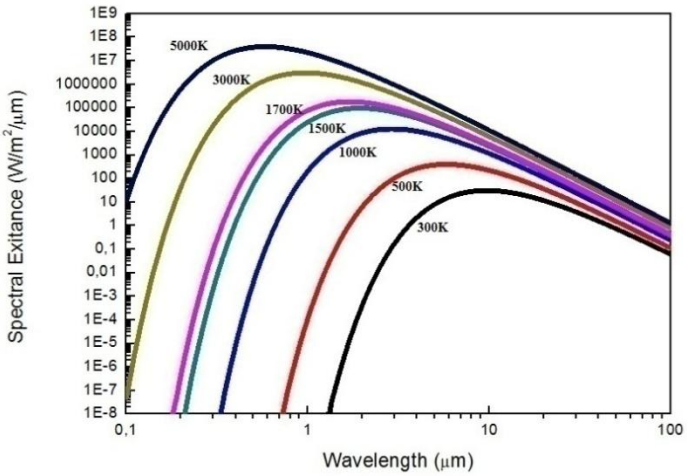

Figure 1.1: Planck's Law for various temperature values

Most properties of infrared radiation can be understood using these three laws. The wavelength window between the 0.7 μm and 1 mm is generally accepted as the infrared range.

The operational wavelength of a detector depends on the application such as medical imaging and can be almost any wavelength for short ranges and high signal intensities. For long range detection purposes such as atmospheric contamination, the medium that the radiation is travelling in is also important besides the operational range of the wavelength of the detector. In atmosphere, some of the molecules that make up the air may absorb IR radiation making it impossible for radiation to reach the detector. Due to their abundance in the atmosphere main absorber molecules are CO_2, H_2O and O_3. However, absorption varies with the energy of the radiation. While these molecules show many absorption bands throughout most of the IR spectrum there are a few in the range of wavelengths where there is no atmospheric absorption. Between the wavelengths of 0.7 μm and 32.0μm, the infrared radiation spectrum is labeled into five transmission windows as:

Near Infrared Radiation	0.7 μm-1 μm
Short Wavelength Infrared Radiation	1μm-3μm
Middle Wavelength Infrared Radiation	3μm-5μm
Long Wavelength Infrared Radiation	8μm-12μm
Very Long Wavelength Infrared Radiation	12μm-30μm

Table 1.1: Wavelength ranges for IR radiation windows.

1.2 Infrared Detection Technologies

The detector should turn IR radiation into some measurable quantity. This measurable quantity is typically electrical. There are basically two types of infrared detectors that make this conversion. First kind is thermal detectors. These detectors are based on the increasing temperature of the detector due to the absorption of energy from the photons that fall on the detector. The change in temperature results in changes on the physical properties of the detector. The physical property can be the resistance (bolometric effect), electric field generation due to the change in dipole moment (pyroelectric effect), pressure in a gas chamber (thermopneumatic effect) and voltage generation on a junction of two different metals (thermovoltaic effect).

Second type of the infrared detectors is photon detectors which are based on the changes in conductivity of the material (photoconductive effect), generated voltage on a junction (photovoltaic effect), voltage generated by the separation of free charged carriers due to an applied magnetic field (photomagnetic effect), kinetic energy of an electron that can make the electron to leave the surface (photoemissive effect).

Photon detectors can be divided into two groups as photoconductive and photovoltaic. Photoconductors are basically made of materials with low conductivity. With absorbed energy from IR radiation, the electrons are excited to the conduction band and conductivity increases. On the other hand, photovoltaic devices are based on the diode structure that is made of p-n junctions of semiconductor materials. These junctions have built-in electric field that separates the photon generated electron-hole pairs. In this way, electrons and holes are sent to opposite sides of the junction and create current. The built-in electric field of semiconductor junctions can be altered with applied bias. In zero bias case, called the photovoltaic mode, the electric field that separates the pairs is used to gather current from the photo generated carriers. This mode is used for solar cell applications. For reverse bias case, which is the photoconductive mode, the electric field difference is increased by an externally applied voltage difference. In this way, the photogenerated pairs separate faster. This process increases the response time of the detector. Inserting an intrinsic type of semiconductor between the p and n types of semiconductor is used for increasing response time even more. The flow of charge carriers from both p- and n-type semiconductors to the intrinsic part generates a high density of carriers that is good for photocurrent generation. Also the intrinsic part of the device acts as the depletion region and it is independent of the applied reverse bias. This wider depletion region compared to p-n junctions makes p-i-n diodes faster [1].

In order to generate an electron-hole pair, electrons should be excited to the conduction band from the valance band with energy from an absorbed photon. The energy of the photon that is to be absorbed and make the electron to pass through the band gap should

at least be equal to the band gap energy. This puts a constraint on the maximum wavelength that can be detected. Minimum wavelength that can be detected by a photon detector is called the cut-off wavelength (λ_c). Cut-off wavelength can be described as;

$$\lambda_c = \frac{hc}{E_{bg}} \tag{1.1}$$

where h is the Planck's constant, c is the speed of light and E_{bg} is the band gap energy.

1.2.1 General Theory of Photon Detectors

Photodetection is based on the principle of current generation upon photon absorption. In a semiconductor p-n junction photodetector,

$$i = i_0 \left(e^{\frac{qV}{bkT}} - 1 \right) - i_g \tag{1.2}$$

where, q is the electronic charge, V is the voltage across the diode, i_0 is the reverse saturation current, b is the nonideality factor, k is the Boltzman constant, T is the diode temperature and i_g is the photogenerated current. The diode is typically operated in the reverse bias. In a realistic case, the detected current will have dark current components in addition to the photogenerated current.

Responsivity is one of the concepts that are used to decide how well a detector is working. Responsivity of the detector defines performance of the detector at turning the incident flux into output current. Responsivity takes the name current responsivity in the case that the incident optical flux is expressed in watts and the output of the detector is in amperes. For photon detectors, in order to define the responsivity, quantum efficiency (η) should also be introduced. Quantum efficiency can be described as the number of generated electron-hole pairs per incident photon. In other words, quantum efficiency defines the quality of the coupling of radiation to the detector and generating photocurrent. It can be defined as;

$$\eta = \frac{I_{ph}}{q\Phi A} \tag{1.3}$$

where I_{ph} is generated photocurrent, q is the electron charge, A is the detector area, Φ is the radiant flux.

With the definition of the quantum efficiency taken into account current responsivity can be defined as;

$$R_i = \frac{\eta q A \Phi}{\Phi_c} \tag{1.4}$$

where Φ_c is the incident photon flux expressed in watts;

$$\Phi_c = hf\Phi \tag{1.5}$$

f is the frequency of the incident light, h is the Planck's constant. Plugging Φ_c into 1.4 current responsivity becomes;

$$R_i = \frac{\eta q A}{hf} \tag{1.6}$$

Specific detectivity (D^*) is the main parameter that characterizes the signal to noise performance of the detectors. Responsivity defines how well the flux is turned into signal but the effect of the noise is missing. Detectivity of a photon detector defines how well the generated signal is read among the noise of the device. Specific detectivity is the ratio of responsivity to noise current with the modulation of area of the detector and bandwidth. Thus specific detectivity is defined as [2];

$$D^* = \frac{R_i (A\Delta f)^{1/2}}{I_n} \tag{1.7}$$

where $R_i$is responsivity, $A_0$is detector area, Δf is bandwidth and I_n is noise. In our case noise is taken as Johnson noise which can be stated as;

$$I_n = \sqrt{\frac{4k_b T \Delta f}{R}} \tag{1.8}$$

where k_b is Boltzmann constant, T is temperature, Δf is bandwidth, R is resistance. Plugging this into the specific detectivity equation results;

$$D^* = R_i \sqrt{\frac{RA}{4k_B T}} \tag{1.9}$$

1.2.2 Detector Types

There are several types of photon detectors. Bulk HgCdTe, InSb, InAsSb, as well as quantum well and superlattice infrared detectors are the ones that found their usages with specific advantages over the others.

HgCdTe IR photodetectors are the most widely used bulk semiconductor devices. The absorption of the photon energy provides transitions between the conduction and valance band of the material. The band structure of the material can be tuned with the alloy composition of the sample. The ratio between Hg and Cd defines the band gap. The band gap of the HgCdTe can be altered to operate in the wavelength range between 1-30 μm. The operating temperature can also be manipulated in the range from 77K to room temperature. However, engineering the ratio between Hg and Cd to tailor the band gap of the material is difficult. For large area production of photodetectors, uniformity of the epitaxial layers is relatively poor. In spite of these drawbacks HgCdTe photodetectors are still the most efficient IR detectors among other competitive technologies.

InSb detectors are also based on the transitions between the conduction and valance band of the material. They are favorable due to the availability of single crystal form. This prevents the problem of uniformity that occurs for HgCdTe. Absence of non-uniformity allows larger focal plane arrays (FPAs). Thermal sensitivity of InSb detectors makes these detectors favorable. The requirement for cryogenic cooling and the deformation of performance over time are the disadvantages of InSb detectors.

InAsSb is also has tunable band gap due to the ratio between As and Sb. Like InSb and HgCdTe the transitions between the electronic bands are the governing system for absorption of energy. The chemical structure makes this material more stable than HgCdTe. InAsSb does not require cryogenic cooling. However, fabrication of the InAsSb is problematic due to the lattice mismatch between InAs and InAsSb. Also, for low percentages, Sb atoms start to act as recombination centers.

Quantum well infrared detectors (QWIPs) are based on the fabrication of quantum wells by putting low band gap material between two layers of a wider band gap material. QWIPs are not bulk devices like HgCdTe, InSb and InAsSb. Absorption occurs between the energy levels inside the well. Therefore, this structure allows band gap

engineering since the energy levels inside the well depend on the size of the well. The applied bias bends the wells and makes it possible for the charge carriers that absorb the energy of the photon tunnel through the barriers to generate a signal.

1.3 Superlattices

A superlattice is an artificial crystal structure that is composed of many successive layers of two different thin single crystal semiconductor materials with different band gaps. It can be defined as a multiple quantum well structure with barrier layers thin enough for tunneling. Superlattice structures shows similarity with the QWIPs in which there are also two materials with different band gaps brought together.

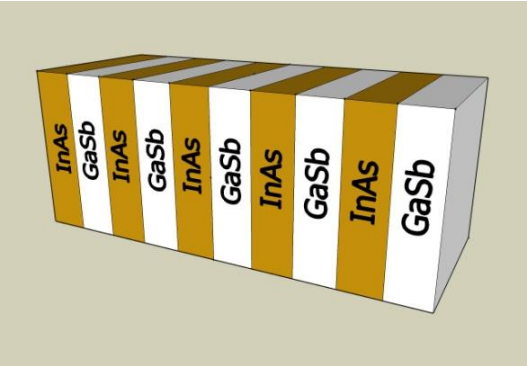

Figure 1.2: Representation of InAs/GaSb superlattice

Superlattices are composed of many multiples of pair of semiconductors with different band gap energies. Superlattices can be characterized by the relative positions of the band gap edges of the different semiconductors with respect to each other. There are three types of such superlattices. In type I superlattice structures, the band edges of the narrow band gap material are located within the band gap edges of the wide band gap material. GaAs/$Ga_{(1-x)}Al_{(x)}As$ superlattice is an example of type I superlattices. In Type II superlattice structures, the band edges of the narrow band gap material partially overlap with the band gap edges of the wide band gap material with the valence band of the narrow band gap material being in between the band edges of the wide band gap material while the conduction band has higher energy. This is staggered Type II superlattice. The second type II structure is the misaligned form. In this structure the conduction band edge of the narrow band gap material is lower than the valence band edge of the wide band gap material. InAs/GaSb system is an example for this type of superlattices.

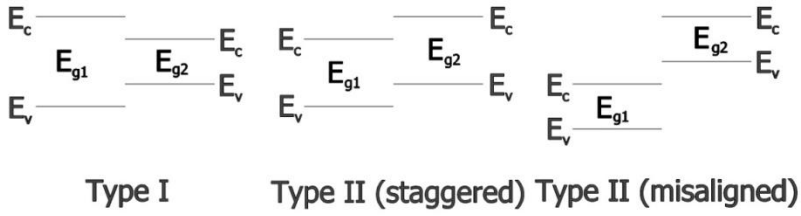

Figure 1.3: Flat band diagrams for different types of superlattice structures

The discrete nature of the band structure changes when a superlattice structure is grown. Unlike the QWIPs where there are discrete energy levels inside the well, superlattices have bands of energy levels due to the fact that the wells and barriers in superlattices are very narrow. This makes the states inside the wells pile up together and form electron and hole minibands. For misaligned type II superlattices, a band gap between hole and electron minibands occurs. The magnitude of this gap depends on the thicknesses of the pairs that make up the periodic structure.

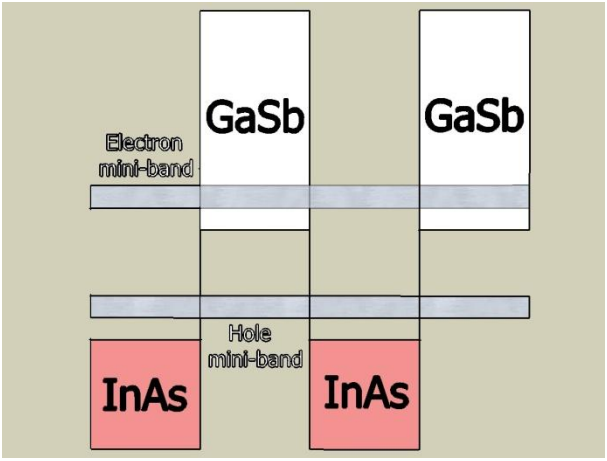

Figure 1.4: Miniband formation in InAs/GaSb superlattice structure

1.3.1 InAs/GaSb Superlattice

InAs/GaSb is a type II misaligned superlattice structure. In this structure the conduction band and valence band edges of InAs layers are lower in energy than the conduction and valence edges of GaSb layers. Thus, electrons and holes are spatially separated with the electrons in the conduction band of InAs and the holes in the valence band of GaSb. InAs/GaSb structure has several features that make it favorable for IR detector applications. Due to the nature of the band structure beyond the scope of this thesis, Auger recombination mechanism is suppressed in the structure [3, 4]. Effective electron mass for InAs/GaSb superlattices is low enough to provide reduced tunneling currents

and large enough to allow good mobility and diffusion length [5]. The band gap of the structure can be calculated and the results show good agreement with the measurements [6].

1.3.2 InAs/GaSb Superlatice Photodetectors

InAs/GaSb type II superlattice structures with their interesting band structure shows promising aspects for IR detection. Formation of minibands and the ability to tailor the band gap between them by appropriate choice of layer thicknesses can be taken as one of these aspects. The InAs/GaSb superlattice detector is based on the generated photocurrent caused by the electrons excited by the absorption of a photon from the hole miniband to electron miniband. As mentioned earlier, p-i-n diode structure is favorable for optical detectors due to the faster response time compared to p-n detectors. For IR detection purposes p-i-n structures can be formed in InAs/GaSb type II superlattice. Also modified versions of p-i-n structures are used for the InAs/GaSb superlattice detectors. There are W-structured, M-structured and nBn type superlattice structures that prove useful for IR detection.

The accumulation of electrons and holes in different layers is another consequence of band structure of InAs/GaSb. Since the electrons and holes are separated, absorption of a photon occurs only at the interfaces between InAs and GaSb. The overlap between the electron wavefunction, which is localized mainly in the InAs layer, and the hole wavefunction, which is mainly localized in the GaSb layer, defines magnitude of absorption. The more the overlap the more the absorption occurs.

A p-i-n InAs/GaSb can be fabricated using a mesa structure with the metal contact on the periphery of the mesa and the bottom of the mesa. Many such devices have been studied. Rehm et al. reports a p-i-n device structure with 5.4 μm cut-off wavelength at 77K. The superlattice structure consists of 190 periods of 9.5 monolayer (ML) thick InAs and 12 ML thick GaSb layers. The lower part of the structure, which is p type, is doped with Be. The upper part is doped with Si atoms to provide n type doping. There is an intrinsic region between p and n-type sections [7]In another paper, two p-i-n structures with 5 μm cut-off wavelength at 77 K and 5μm at room temperature is designed and compared. For 5 μm cut-off wavelength at 77 K, 9 monolayers (ML) of InAs and 10 ML of GaSb are used. For room temperature the diode is designed with 8 ML of InAs and 11 ML of GaSb [8]. A 7 μm cut-off wavelength p-i-n structured InAs/GaSb is reported which is defined with 9 ML of InAs and 4 ML of GaSb. InAs layers are doped with Be to define the p side and GaSb is doped with Si to define the n side of the diode [9]. Another p-i-n structured InAs/GaSb superlattice photodiode is reported with 11 μm cut-off wavelength. The p and n sides of the diode is composed of 14.36 ML of InAs and 7.35 ML of GaSb. The n side is made of 14.36 ML of InAs and

6.90 ML of GaSb. Be and Si are used as the dopants as in the previous paper [10]. 12 μm cut-off wavelength is reported for InAs/GaSb superlattice photodiodes with the 13 ML of InAs and 7 ML of GaSb design. Si and Be is used as dopants for n and p type doping respectively [11]. The best results on T2SL IR detector with simple pin architecture has been reported by Cervera et al in J. Electron. Mater.41(10), 2714, 2012. At 77K, the dark current density as low as $6.2x10^{-8}$ A/cm^2 at -50mV and R_0A product higher than $1x10^6\Omega cm2$ has been measured (4.55 μm cut-off wavelength at 77K). [12]

W-structure superlattice is first proposed by Meyer et al [13]. The reported structure is in the form of GaAlSb/InAs/GaInSb/InAs/GaAlSb. The band structure looks like a W letter, from which the name comes. The large band gap of GaAlSb is used as a barrier. Since there is a barrier the electron wavefunction in the InAs is tilted towards the GaSb layer from both sides. This tilt from both sides increases the overlap between wavefunctions and electronic confinement. The overlap increase results increase in absorption. Also the density of states can be taken as 2D instead of 3D [13]. The usage of W structure for dual band photodiodes is reported [14]. The usage of AlGaInSb is also reported as the barrier material and higher quantum efficiency is achieved for LWIR [15]. Also it is reported that application of graded band gap to W-structured Type II superlattices results in dark current suppression[16].

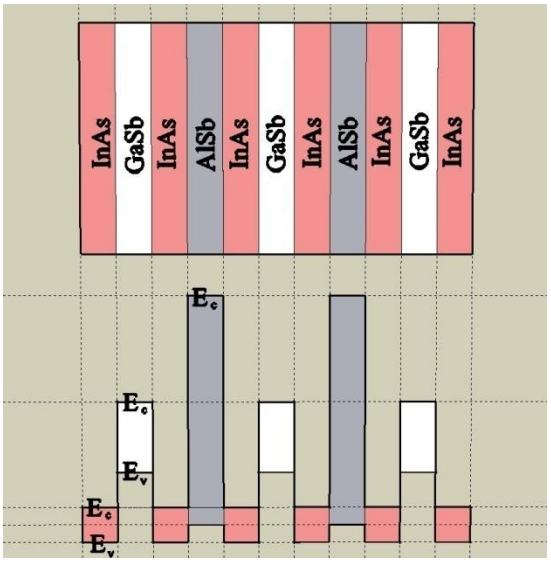

Figure 1.5: Flat band diagram for W-structure superlattice composed of InAs, GaSb, and AlSb. AlSb is used as barrier layer.

M-structure superlattice is formed by the injection of a large band gap material as a barrier in the middle of the GaSb layer. AlSb is reported as the barrier material. This injection increases the stiffness of the band structure and provides higher carrier effective mass. Like in the W-structure this barrier decreases the dark current and

increases the overlap electron and hole wavefunctions. Also the barrier divides the GaSb well into two and consequently changes the valance band energy. Besides these features this structure continues to show favorable behaviors like suppression of Auger recombination. Since the lattice mismatch between AlSb and GaSb is small this structure does not require additional growth precautions [17]. These features of the M structure are useful for suppression of diffusion and tunneling current that are increasing the dark current. M-structured type II InAs/GaSb superlattice long wave photodiodes are reported to show higher zero bias area resistance values than structures without barrier[18]. The effect of optimization of the doping of M barrier is also investigated and the results are promising for the usage of this structure for VLWIR detection [19].

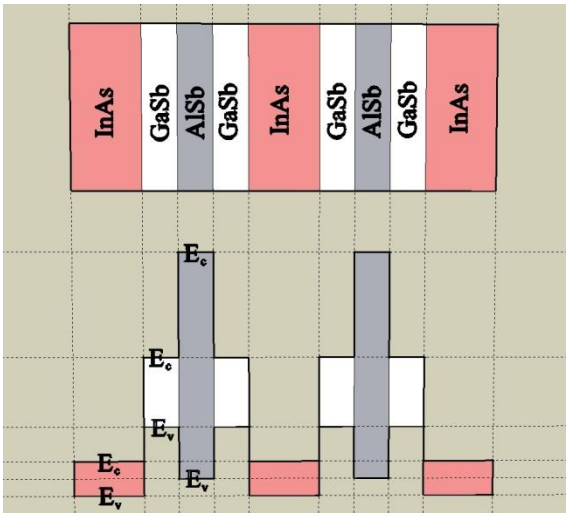

Figure 1.6: Flat band diagram for M-structure superlattice composed of InAs, GaSb and AlSb. AlSb is used as barrier layer.

nBn structured devices first designed for bulk InSb and InAsSb detectors with the aim of filtering the photogenerated minority carriers for detection [20]. With this approach, the Shockley-Read-Hall current is suppressed and the dark current is reduced. Also the definition of the device can be made with a shallow etch which ends at the barrier level. With this method the active region of the detector is protected by the barrier. The use of InAs/GaSb type II superlattice structures instead of bulk materials results in comparable results[21]. Two orders of magnitude decrease in dark current is reported for the shallow etched detectors compared to conventionally etched devices[22]. A similar structure to the nBn structure, pBp structure, is also reported. Instead of blocking the majority carriers (electrons) and passing the minority carriers (holes), pBp structures allow majority carriers and blocks minority carriers. pBp structures are reported that they show better performance than the QWIPs and comparable performance with HgCdTe devices [23].

While interesting band structures are being used to achieve low dark currents, and high operating temperatures, these approaches ultimately complicate the crystal growth as

well as fabrication technology, increasing cost. Lowering dark current in the simplest diode configurations remains to be a challenge. Surface passivation to lower surface leakage currents is the objective of this thesis.

1.4 Device Processing and Surface States

InAs/GaSb superlattice pin detectors studied in this thesis are fabricated by etching a well defined mesa on the surface of the superlattice crystals. The size of the mesa may range from 25x25 μm^2 to 1000x1000 μm^2. The mesa confines the electrical current to be measured. This approach results in the abrupt ending of the crystal structure on the mesa walls. This results in additional energy states in the band gap of the crystal located on the surface. These are called surface states. These states in the band gap cause recombination and decrease the signal as well as forming conduction channels for the photoelectrons close to the surface. Surface states, therefore, can affect the performance of the detectors, significantly. Impurities on the surface can also generate surface states. These impurities might be anything that does not belong to the crystal. Defects, dangling bonds due to surface atoms on the mesa sidewalls and oxides of the materials can be taken as the main sources of the surface states. Passivation can be described as any process that can minimize the surface states and therefore decrease the surface leakage current. The passivation layers should chemically and electronically passivate the surface. The passivating layer should not interfere with the photogenerated current and ultimately should decrease the dark current of the device.

In the case of InAs/GaSb, the sources of surface states can be defects, dangling bonds and native oxides of the Ga, In, As and Sb. Since these elements are chemically very reactive, an oxide layer forms almost instantly. Some of these oxides can be electrical conductors and can act as current channels. Defects, dangling bonds and these oxides cause surface leakage currents and decrease the device performance. In order to eliminate or minimize surface leakage, these surface states should be minimized. For the passivation of InAs/GaSb type II superlattice IR detectors, two passivation techniques are proposed as the core of this thesis, atomic layer deposited Al_2O_3 and octadecanethiol passivation.

For most infrared radiation detection applications focal plane arrays are used. A focal plane array is a matrix of detectors optically and electrically isolated from each other and integrated on the same chip. Each detector is called a pixel. Increasing the number of pixels on the same size chip requires smaller detectors. Shrinkage in the size of detectors increases the problem of surface leakage current.

In Chapter 2 we present background information about InAs/GaSb type II superlattice structures. The features of the structure that makes it favorable for IR detection will be explained briefly. Working principles of an InAs/GaSb superlattice detector will be explained through a presentation of the miniband structure, accumulation of different charge carriers on different layers and the effect of this situation on absorption. Finally, the general dark current mechanisms such as diffusion current, generation-recombination current and tunneling current, will be defined. Surface states that cause surface leakage current will be described. Then there will be a background survey for the passivation techniques used so far for InAs/GaSb superlattice structures. The methods that will be covered are passivation by deposition of dielectric materials, sulphur passivation, polyimide passivation and passivation with the overgrowth of a large band gap material. At the end of the chapter the proposed passivation methods that are ALD Al_2O_3 and ODT SAM passivations, will be explained and the reasoning for the choice of these methods will be given.

In the third chapter the superlattice structure that we used for our device processes will be introduced. Since our crystals were grown by the molecular beam epitaxy (MBE) technique there will be basic information about MBE. The fabrication process that we used to define our detectors will be described. The setup used for I-V measurements, both temperature dependent and at constant temperature will be explained. Spectral responsivity measurements and the setup will also be introduced.

In chapter four the effects of ALD Al_2O_3 passivation and ODT SAM passivation will be given. The dark current reduction effects of both passivation techniques will be shown for 77K. There will also be temperature dependent measurements for both passivation techniques. Additionally, since the ODT SAM is sulphur based passivation technique time dependent dark current measurements will also be given in order to check the degradation effect on the dark current. The comparison between ALD Al_2O_3, ODT SAM, SiO_x, SiN_x passivations will be made.

Chapter 2

Background

In this chapter we will first present the features of InAs/GaSb superlattice that make the structure favorable for infrared detection. The operating principles of an InAs/GaSb photodetector will be discussed. Figures of merit and general dark current mechanisms for the photodetectors will be explained. Passivation techniques that are used to reduce dark current in InAs/GaSb superlattice photodetectors will be covered. Atomic layer deposited Al_2O_3 and octadecanethiol will be introduced as passivation techniques. The reasoning for these passivation techniques will be discussed.

2.1 Favorable Features of InAs/GaSb Superlattice Detectors

There are mainly three advantages of InAs/GaSb superlattice structures for IR detection. First one of these advantages is the ability for band gap engineering. The superlattice consists of tightly packed thin quantum wells separated with thin barriers forming a semiconductor structure with an artificial period. As is well known, the energy levels of a quantum well are related with the width of the well. In a superlattice, tightly spaced numerous subbands for electrons and holes form an energy band (miniband) where the effective band gap of a superlattice structure is the difference between the upper edge of the hole miniband and lower edge of the electron miniband which can be tuned by controlling of the width of the thin layers. The band structure of an InAs/GaSb superlattice can be calculated with good agreement with the experiments using the empirical tight binding method, with the adaptation of the segregation of elemental Sb into the InAs layers[6]. This control over the band structure makes the InAs/GaSb superlattice structure a good candidate for detection of a wide range of the IR spectrum due to the ability to engineer the band gap. As the period of the superlattice increases,

the energy difference between the edge of the electron miniband and the hole miniband decreases. [24] Thus, the cut-off wavelength of an InAs/GaSb type II superlattice photodetector can range from 4.5 μm to 32μm for various temperatures [8-11, 16, 18, 25-28].

Second advantage of photodetectors made with InAs/GaSb superlattice is the suppression of the Auger recombination mechanism. Auger recombination is an intrinsic recombination mechanism. Basically, it occurs during recombination of an electron with a hole. The energy from this recombination is taken up by another conduction electron to be excited to a higher energy state. Excited electron relaxes to the bottom of the conduction band through scattering with phonons. Auger recombination mechanism may also be seen between the states in the band gap. However, the most important type is the band-to-band Auger recombination for small gap materials. Since our superlattice detectors have small band gaps, suppression of Auger recombination mechanism is crucial for device performance. Fortunately, the size of splitting between the heavy hole band and light hole band in $In_{(x)}Ga_{(1-x)}Sb/InSb$ superlattice structure is larger than the energy gap[3]. Thus the energy from the relaxation of an electron from conduction band to heavy hole band is insufficient to excite an electron from the light hole band to heavy hole band. This situation increases the Auger life time [4]. Similarly, the energy difference between the heavy hole band and split hole band is larger than the band gap energy [13]. This prevents the excitation of an electron from the split-off band to the heavy hole band with the energy gathered by the relaxation of an electron from conduction band to heavy hole band. With these two energy level alterations in InAs/GaSb type II superlattice the CHSH (recombination by the energy transfer from a conduction band to heavy hole band relaxation to an excitation from split-off band to heavy hole band) and CHLH (recombination by the energy transfer from a conduction band to heavy hole band relaxation to an excitation from light hole band to heavy hole band) Auger recombination mechanisms are suppressed. This suppression increases the Auger lifetimes.

Third feature that makes the InAs/GaSb superlattice is the effective electron mass. The electron effective mass is $0.04m_0$ InAs/GaSb system [5]. This value is nearly isotropic. Compared with HgCdTe, this value is large enough to reduce diode tunneling currents. Also, it is small enough to provide good mobility and diffusion length.

2.2 Operating Principles of InAs/GaSb Superlattice Photodetectors

InAs/GaSb superlattice structure is distinguished with its misaligned type II band formation. In this structure, the conduction band edge of the InAs layer is positioned below the valance band edge of the GaSb layer. This band structure provides electronically favorable features for photodetector design.

One of the interesting consequences of the type II misaligned band structure of InAs/GaSb is the separation of different charge carriers in different layers. Due to the potentially favorable InAs layers, electrons in the superlattice are concentrated on these layers. Similarly, holes of the superlattice structure are accumulated on the GaSb layers. Due to this separation interfaces between the InAs and GaSb are the only places for the photon absorption to occur. The overlap between the electron and the hole wavefunctions at interface between the layers can be defined. In order to excite an electron with a photon, electron should be spatially close with a hole, meaning their wavefunctions should overlap. The separation of electrons and holes in different layers leads to a decrease in the overlap of electron and hole wavefunctions. The overlap of electron and hole wavefunction is important for absorption of photons. For small overlap between wavefunctions the possibility of electron to absorb the photon and be excited is low. The absorption of a photon, therefore, takes place between these minibands. An electron from the hole miniband is excited to the electron miniband with the energy absorbed by photon.

It is a challenge to design structures to increase the overlap integral of the electrons and holes in order to increase optical absorption and therefore the quantum efficiency. There are special superlattice designs to increase the electron and hole wavefunctions, like W structured superlattices [13].

The band gap energy defines the energy, therefore the wavelength, of the radiation to be detected. However, the overlap between the wavefunctions determines how likely it is for the superlattice to absorb the photon.

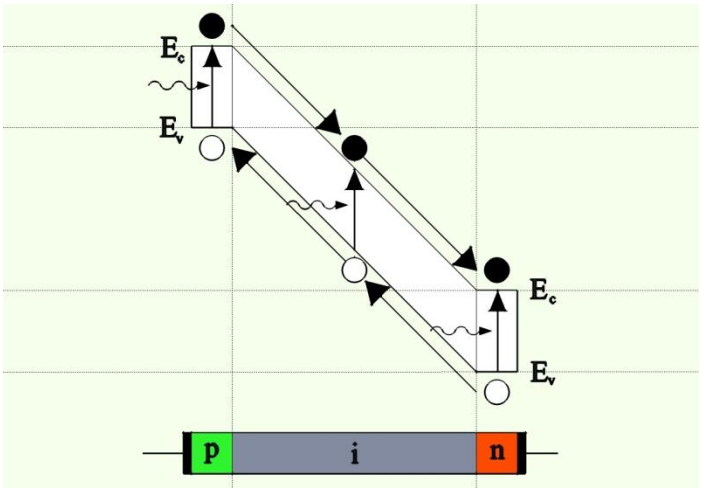

Figure 2.1: Cross-sectional view and energy band diagram of a p-i-n diode.

2.3 Dark Current Mechanisms

The figures of merit for a photodetector were given in Chapter 1. Since the detectivity of a detector is defined due to the performance with the noise mechanisms taken into account, these mechanism should be characterized and understood. The dark current mechanisms for InAs/GaSb superlattice detectors can be taken as; Diffusion current (I_{Diff}), generation-recombination current (I_{G-R}), band-to-band tunneling (I_{btb}), trap assisted tunneling (I_{tat}) [29-31].

2.3.1 Diffusion Current

Diffusion current, or specifically bulk diffusion current, occurs due to the thermally generated minority carriers present near the depletion region of a junction. Minority carriers which are at a distance of at least a diffusion length to the depletion region flow through depletion region to provide charge neutrality on the junction. Bulk diffusion current can be expressed as [29];

$$I_{Diff} = I_0 T^3 \exp(-E_g/kT)\left[\exp\left(\frac{qV}{kT}\right) - 1\right] \tag{2.1}$$

where I_0A is a constant independent of temperature and bias voltage, E_g is the band gap of the material, k is the Boltzmann constant, T is the temperature and V is the bias voltage. I_0 can be defined as [29];

$$I_0 = Aq\left(\frac{D_e n_i^2}{L_e N_A} + \frac{D_h n_i^2}{L_h N_D}\right) \tag{2.2}$$

where A is the detector area, D_e and D_h are electron and hole diffusion coefficients respectively, L_e and L_h are electron and hole diffusion length respectively, n_i is the intrinsic carrier concentration. As can be seen in these two equations the diffusion current originates from the temperature and effective for both forward and reverse bias. Diffusion current is not a photocurrent.

2.3.2 Generation-Recombination Current

There are three basic recombination mechanisms. First one is the band-to-band recombination which occurs due to the relaxation of an electron from the conduction band to an empty state in valance band. This is an intrinsic recombination mechanism.

Another intrinsic recombination mechanism is Auger recombination which is mentioned above. The third generation-recombination current is caused by defects in the depletion region of the junction that act as recombination centers for generated electron-hole pairs. This mechanism is an extrinsic one. Any defect inside the material can form an intermediate state inside the band gap. These intermediate states make it easier for photogenerated electron-hole pairs to recombine since they are energetically favorable to reach. In short, defects inside the depletion region may prevent the photogenerated current to reach the junction and causes thermally generated currents. This mechanism is called Shockley-Read-Hall recombination mechanism.

Generation-recombination current can be modeled as [29];

$$I_{G-R} = CT^{3/2} \exp\left(-E_g/2kT\right) (V_b - V)^{1/2} [exp(qV/2kT) - 1] \quad (2.3)$$

where C is a temperature independent coefficient.

2.3.3 Tunneling Current

Tunneling current in diodes occurs through two mechanisms. First one of these is the band-to-band tunneling which is caused by band bending due to the applied bias. Second one is the trap assisted tunneling which is based on the trap states inside or near the depletion region. These trap states acts as a ladder for carriers to reach conduction band.

2.3.3.1 Band-to-Band Tunneling

Band-to-band tunneling occurs due to the band bending which is caused by the applied bias. When reverse bias is applied to the diode the conduction band of a well can be aligned with the valance bend of a neighboring well. If the thickness of the well is small tunneling can take place. Since superlattice structures are multi well structures with very thin barriers this mechanism can be effective for superlattices. Charge carriers from the valance band can tunnel through the conduction band and pass the junction and generate current. The applied reverse bias is directly effective on this mechanism. Higher reverse bias values increase the alignment and consequently increase the tunneling current. Band-to band tunneling can be modeled as;

$$I_{btb} = \frac{\sqrt{2m_e^*}q^3EV}{4\pi^2\hbar^2\sqrt{E_g}} exp\left[\frac{-4\sqrt{2m_e^*}{E_g}^{3/2}}{3qE\hbar}\right] \quad (2.4)$$

Wherem_e^* is electron effective mass, q is electron charge, V is applied voltage, E_g is band gap, E is maximum electric field [[1]].

2.3.3.2 Trap Assisted Tunneling

Trap assisted tunneling occurs due to the transitions through the trap states that are energetically close to the valance band. With the thermal excitation the charge carriers jump to the trap states from the valance band. After that charge carriers make tunneling and jump to an empty state in the conduction band. Trap-assisted tunneling can be stated as;

$$I_{tat} = \frac{q^2Vm_e^*M^2N_t}{8\pi\hbar^3} exp\left(-\frac{4\sqrt{2m_e^*(E_g - E_t)^3}}{3q\hbar E}\right) \quad (2.5)$$

Where N_t is activated trap density, M^2 is matrix element associated with trap potential,E_t is trap state energy [32].

2.3.4 Surface Leakage Current

Surface leakage current occurs due to the surface states that are mainly caused by the surface itself. The change in the periodic structure of a semiconductor crystal allows surface states to occur. The surface can be generated by the abrupt ending of the crystal. The interface between the crystal and the vacuum causes surface states. Also the impurities on the surface can generate surface states. These states cause intermediate energy states inside the band gap and allow thermally generated transitions to take place besides optical ones.

For InAs/GaSb superlattice photodiodes in order to define the diode the crystal structure should be etched to define the mesa structures. This etch process causes abrupt ending of the crystal which causes surface states These are dangling bonds that are generated by the mesa etch. The unsatisfied bond of the crystal acts as a current channel and contributes to the surface leakage current. Also In, As, Ga and Sb are chemically very reactive materials. The oxides of these materials form on the mesa side walls will almost instantly oxidize. Some of these oxides are conductors and these conductor oxides can cause leakage current. The passivation technique to be used to minimize

surface leakage current for InAs/GaSb superlattice photodiodes should eliminate the oxides on the surfaces, satisfy dangling bonds, electrically and chemically isolate the surface and ultimately should decrease the dark current level.

2.4 Passivations Used

There are several methods that were proposed to decrease the surface leakage current on III-V devices. Growth of dielectric materials on the surfaces, chalcogenide (sulphur, selenium) passivation, polyimide passivation and the overgrowth of wide band gap materials are the techniques that prove useful for passivation of superlattice detector passivation[33-38]. As the first method, deposition of thick dielectric materials can be used for passivation. The dielectric material can be native oxides, nitrides of the materials that the device is made of, or other foreign materials. This thick dielectric layer is expected to cover the surface and prevent the surface to interact with the ambient atmosphere. This way the current channels are prevented from carrying charges. However, the temperatures that are required for the deposition of these oxides or nitrides are close to the growth temperature of the device material. Therefore, this method can be harmful for the device structure. Also the band gap difference between the device and the passivation can cause the band bending which can change the device characteristics. Generally used dielectric materials are SiO_2 and SiN_x [37, 38]. Second, coating the surfaces with chalcogenide materials has been reported as a possible passivation technique. Sulphur stands out among other chalcogenides. There are a lot of materials that are used as the source of the sulphur as well as many different ways for deposition of the sulphur on the surface of the device [33, 34, 39]. Sulphur satisfies the dangling bonds on the surface and also exchanges with the oxygen to reduce the native oxides on the surface [40]. Therefore, it decreases the density of the surface states inside the band gap. This helps to reduce the leakage current. On the other hand, chalcogen passivation effect degrades over time through the interaction with ambient temperature[38]. The generation of a long lasting encapsulating layer requirement is not satisfied by this type of passivation. Third passivation method that was introduced is the use of polyimide to passivate detectors. Polyimide material effect on decreasing the leakage current does not degrade over time[35]. Finally over-growth of wide band gap semiconductor is also used as a passivation layer. This seems a reasonable method since the passivation should electrically isolate the structure. There are problems about the application of this passivation. The semiconductor that is used for the passivation should have appropriate lattice constant to prevent lattice mismatch. The surface that the passivation is applied to should be cleaned carefully before the process. The passivation of InAs/(GaIn)Sb superlattice photodetectors by epitaxially grown $Al_{(x)}Ga_{(1-x)}As_{(y)}Sb_{(1-y)}$ has been reported[36].

2.5 Proposed Dark Current Control Methods

We propose two passivation techniques to be applied to Type II InAs/GaSb superlattice photodetectors. First one is the atomic layer deposited (ALD) Al_2O_3 passivation. In this method, favorable Gibbs free energy for the formation of Al_2O_3 is expected to provide self cleaning of the device sidewalls and also chemically and electronically passivate them. Second method is the coating of the exposed surfaces with octadecanethiol (ODT), $CH_3(CH_2)_{17}SH$. ODT is a molecule with a sulphur atom at the head of a hydrocarbon chain. ODT generates self assembled monolayers (SAM) on the surface. As the long carbon chains are attached to a sulphur atom, this method resembles the sulphur passivation.

2.5.1 ALD Al_2O_3 Passivation

Most photodetectors are etched in the form of a mesa in order to confine the photocurrent. During the etch process to generate mesa structures, the abrupt ending of the crystal structure leaves surface atoms asymmetrically bonded to the surface (dangling bonds). These bonds can act like current channels. Also, the elements that the InAs/GaSb superlattice structures composed of are chemically very reactive. Native oxides of these elements can form on the mesa surfaces. Some of these oxides are conductive and also generate current channels and contribute to the surface leakage current. Elimination of these oxides may result in the decrease of the leakage current. The Gibbs free energy of the possible oxides that can form on the surface are -75.3 kcal/mol, -238.6 kcal/mol, -198.6 kcal/mol, -137.7 kcal/mol, -187 kcal/mol, -151.5 kcal/mol for Ga_2O, Ga_2O_3, In_2O_3, As_2O_3, As_2O_5, Sb_2O_3 respectively[41, 42].The Gibbs free energy for Al_2O_3 is -377.9 kcal/mol[43]. Due to this difference in the free energy values, reduction of Ga, As, In and Sb oxides are expected and Al_2O_3 is favored to form. The reduction of Ga and As oxides on etched surface of GaAs by the formation of Al_2O_3 is reported through X-ray photoelectron spectroscopy (XPS) [44]. XPS measurements also show that formation of Al_2O_3 occurs through the reduction of In and As oxides[45]. Electrical characterization of MOS capacitors that are made of Sb based crystals and XPS measurements are used to confirm Sb native oxide reduction on GaSb crystals. Again Al_2O_3 formation seems to be preferred chemically[46].

The ALD technique is favorable for the passivation since it is working in a cyclic manner depositing each atomic layer one at a time. The number of cycles helps to decide the thickness of the passivation layer in molecular level. Also the required temperature for operation during the deposition is low compared to the growth temperature of the crystal and there is no plasma that can damage the structure. Al_2O_3 is a good dielectric over a very large frequency range.

2.5.2 Octadecanethiol Passivation

ODT SAM passivation is expected to be effective as a passivation layer in the way that the sulphur passivation works. The native oxide forming on the sidewalls of the mesa structure degrades the device performance as acting like current channels. Elimination of these oxides is crucial. Replacement of oxygen with sulphur is the main principle of sulphur passivation. However, the aging effect of the classical sulphur passivation makes it undesirable. In sulphur passivation encapsulation requirement is missing. During the deposition of sulphur, the crystal to be passivated may be damaged[37].This type of harmful effects of sulphur passivation on samples are not observed for ODT [47]. ODT SAM includes a reactive sulphur head and a carbon chain which composed of 18 atoms. The sulphur on the head shows the same behavior as in other sulphur methods that reduce the native oxides, prevents new oxide re-growth and satisfies the dangling bonds on the surface. Measurements with high resolution X-ray photoelectron spectroscopy (HRXPS) and time-of-flight secondary ion mass spectrometry (ToF-SIMS) show that the application of ODT SAM results in mainly in As-S bonds and minor Ga-S bonds on the surface[48]. Similarly for InAs surfaces the effects of ODT SAM is investigated by a wide range of techniques in the paper by Knoben et al[49].

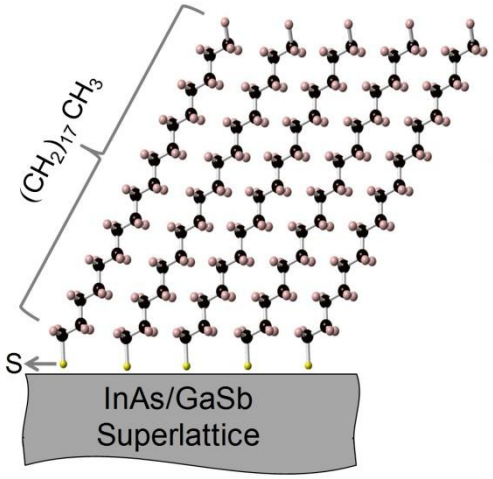

Figure 2.2: Schematic representation of ODT deposited on InAs/GaSb superlattice.

The application of the ODT to the surface is made by dipping the samples in a solution containing ODT. This makes it easy to apply.

Chapter 3

Materials and Experimental Methods

In this chapter we present the design details of crystals that we used to define p-i-n photodiodes followed by a brief explanation on the molecular beam epitaxy technique used to grow these crystals. Then the device processing we use to fabricate photodiodes will be explained. The fabrication processes for both ALD Al_2O_3 passivated and ODT SAM passivated samples will be covered. Finally, the measurement setups for I-V measurement, temperature dependent I-V measurement and responsivity measurement will be introduced.

3.1 Design of InAs/GaSb SL Photodiode

The design of the pin photodiodes start with the selection of cutoff wavelength. The cutoff wavelength was chosen as 5 μm. The thickness of InAs and GaSb to achieve a 5μm cutoff wavelength is well known in the literature [8, 28]. To obtain a p-i-n structure p and n-type doping is achieved by doping InAs n-type and GaSb layers as p-type. In the intrinsic region, no doping is used. The thickness of n and p-type layers is chosen to 291 nm and 437 nm for Al_2O_3 passivated samples, 291 nm and 680 nm for ODT SAM passivated samples respectively. The thickness of the intrinsic layer can be as large as possible and is limited by the cost of the growth. The samples for ALD Al_2O_3 passivation is designed as a p-i-n diode with 5 μm cut-off wavelength. The structure is started with a buffer layer which is 100 nm thick GaSb layer. After that there is a 20 nm thick Al(x)GaAsSb(y) as an insulating layer and etch stop layer. On top of this insulating layer there is a 1000 nm thick GaSb:Be (p:$1.0 \times 10^{17} cm^{-3}$) p contact layer. Then the p-i-n structure begins. The p-i-n diode is defined by 90 periods 8 MLs of InAs/8 MLs of GaSb:Be (p: $1.5 \times 10^{17} cm^{-3}$) as p layer, 60 periods 8 MLs of InAs/8

MLs of GaSb as i layer and 60 periods 8 MLs of InAs:Te (n:$5 \times 10^{17} cm^{-3}$)/8 MLs of GaSb as n layer. Finally, there is a 20 nm thick InAs:Te (n:$5 \times 10^{17} cm^{-3}$) layer to provide good ohmic contact.

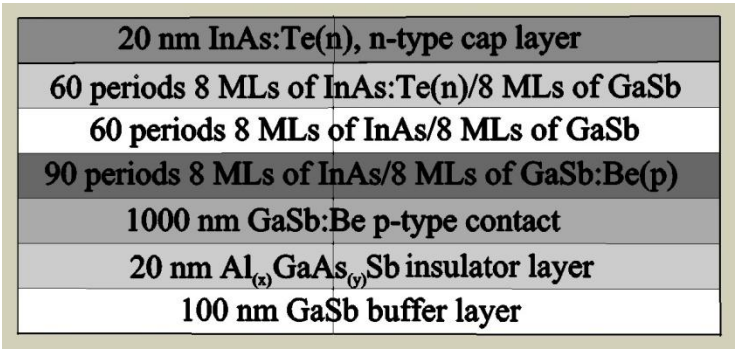

Figure 3.1: Superlattice p-i-n diode structure used for Al_2O_3 passivated sample fabrication.

The samples that are used for ODT SAM passivation is also designed as a p-i-n diode with 5 μm cut-off wavelenght. As a buffer layer there is a 100 nm thick GaSb buffer layer and 20 nm $Al_{(x)}GaAs_{(y)}Sb$ as an insulator and etch stop layer, followed by 1000 nm GaSb:Be (p=1.0x10^{17} cm^{-3}) p contact layer. The p-i-n part of the design is composed of 140 periods 8 MLs of InAs/8 MLs of GaSb:Be (p=1.5x10^{17} cm^{-3}) as p layer, 40 periods 8 MLs of InAs/8 MLs of GaSb as intrinsic layer, 60 periods 8 MLs of InAs:Te (n: 5x10^{17} cm^{-3})/8 MLs of GaSb as n layer. Finally, the structure is terminated with 20 nm InAs:Te (n: 5x10^{17} cm^{-3}) cap layer for good ohmic contact.

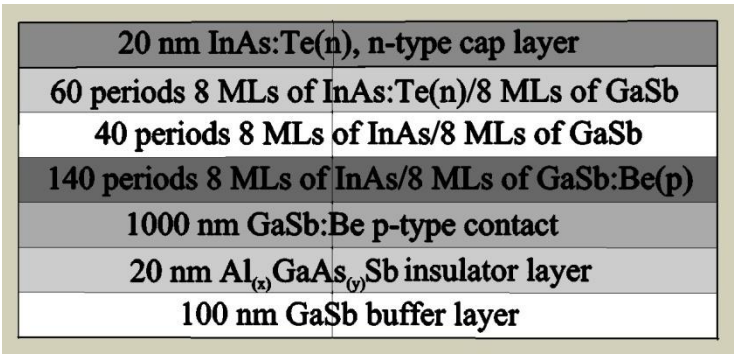

Figure 3.2: Superlattice p-i-n diode structure used for ODT SAM passivated sample fabrication.

The crystals that we use for fabricating our samples for this study were grown commercially (IQE Inc. USA) with molecular beam epitaxy (MBE). A brief explanation of this crystal growth technique follows.

3.1.1 Molecular Beam Epitaxy

The growth of very thin layers of InAs and GaSb on top of each other starts with choice of the substrate. GaSb substrates are routinely used for this purpose. The epitaxial layers can be grown by MOCVD or MBE techniques. Epitaxy is a single crystal growth method that is based on the usage of another single crystal as seed. The film that is growing on the substrate duplicates the lattice structure of the seed crystal. There are basically two types of epitaxy methods which are liquid phase and vapor phase epitaxy. In both MBE and MOCVD method, epitaxial growth takes place in the vapor phase epitaxy in which the atoms or molecules are used to form the thin film on the substrate. MBE is a kind of vapor phase epitaxy. In order to deposit thin films on the heated substrate crystal, atomic or molecular beams are directed towards the substrate under ultrahigh vacuum conditions. They fall on the substrate to form the thin film.

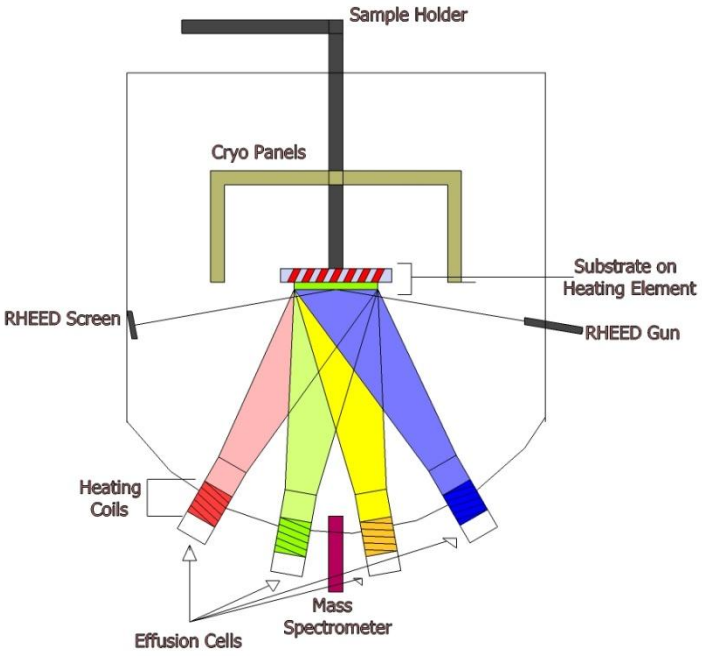

Figure 3.3: Schematic representation of MBE growth chamber.

An MBE system is composed of ultra high vacuum chambers able to achieve vacuum levels down to 10^{-11} Torrs. The vacuum of the chambers are provided by ion pumps or cryo pumps. Also liquid nitrogen cooled panels are used to trap the molecules that are present inside the chamber. Since these panels are cold the molecules that hit the panels sticks to panels. In order not to break the vacuum to insert the sample an interlock system is used. Knudsen effusion cells are used to generate the atomic or molecular beams. Temperature of cells that contain different materials is controlled independently. There are shutters for each cell in order to control the flux of each material with the help of an ion gauge. A reflection high energy electron diffraction (RHEED) unit is used to

monitor the growth [50, 51]. MBE approach to crystal growth is able to achieve monolayer thickness control. Once the crystals are grown, they are quality checked with high resolution X-ray diffraction. Using a double crystal X-Ray diffraction technique it is possible to check the thickness of each layer, total thickness as well as their composition. Possible strain in the layers can also be determined.

3.2 Fabrication of Device

The fabrication process of InAs/GaSb superlattice photodiodes are same for both ALD AL_2O_3 passivated and ODT SAM passivated samples except for the passivation step. The device process starts with the cleaning of the sample with acetone, methanol and isopropyl alcohol with this order. Then the sample is rinsed with water and blow dry with N_2. After cleaning, sample is put into the spinner and spun with AZ5214E image reversal photoresist. In a two step program sample is rotated first with 500 rpm for 5 seconds and then with 5000 rpm for 55 seconds. Approximate photoresist thickness on sample is 1,4 μm. In order to turn the photoresist into UV exposable state, sample is baked for 55 seconds at 110 ºC. Now sample is ready for the photolithography step.

In order to transfer a pattern to the photoresist spun on sample surface, specified areas on the surface are exposed with UV light and other areas should be masked. For this purpose we design masks using L-Edit software. There are three mask levels that are used in order to determine the devices on the sample crystal. First of the masks that are used is the “etch mask” which is used to define the mesa structures. Second one is the “passivation mask” which helps to limit the passivation layer only on the mesa side walls. Third and the last mask is the “metallization mask” which is used for coating gold on specified areas of the devices. Each mask that we designed consists of six 100x100 μm^2, six 200x200 μm^2, eight 300x300 μm^2, seven 400x400 μm^2, eight 500x500 μm^2, six 600x600 μm^2 and four 700x700 μm^2 sized structures on each 5mm*5mm array for Al_2O_3 passivated samples. The mask that is used for ODT SAM passivated samples consists of sixteen 400x400 μm^2, ten 500x500 μm^2, and ten 600x600 μm^2 sized structures. The total area of each mask is 1cm1cm. There are four equivalent device layouts on this mask area. This way we can fabricate four separately measurable detector arrays in one process.

For the first expose on the sample, etch mask is used. The expose time is about 78 seconds. After UV expose, sample is dipped into the developer solution for about one minute. This solution is prepared with AZ400K developer and water in the ratio of 1:4, respectively. UV exposed sides of the photoresist becomes soluble in the developer solution. Since our mask blocks t UV light with square patterns, square features made of photoresist stays on the crystal and all the other parts are cleared off the photoresist. The square shaped photoresist will be used as a protective layer against the etch acid. In

order to make the photoresist on the surface of the sample stronger against the etching acid, sample is baked further at 125 º about 150 seconds. The thickness of the photoresist on the sample is measured with DEKTAK profilometer in order to decide the etch depth. After this step the sample is ready to be put into the etch solution.

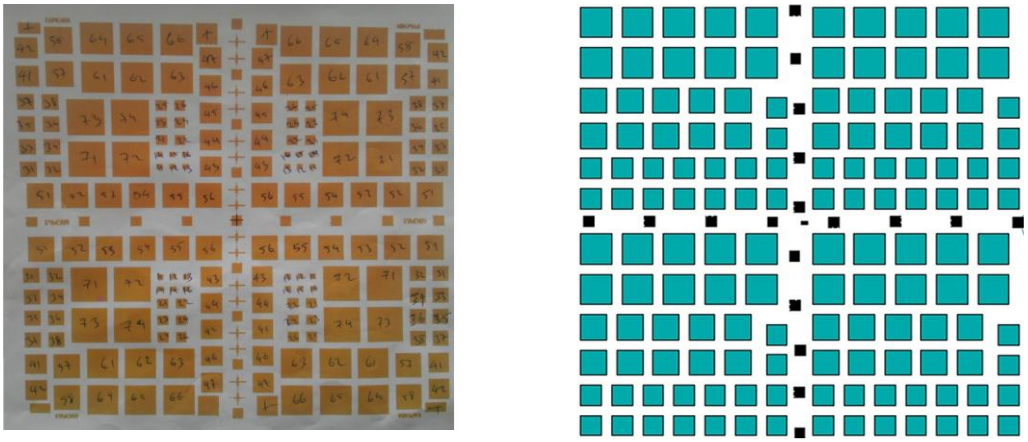

Figure 3.4: Device layout for the mask that is used to fabricate ODT SAM passivated samples (right) and ALD Al_2O_3 passivated samples (left).

The etching recipe is composed of water (H_2O), ortho-phosphoric acid (H_3PO_4) and hydrogen peroxide (H_2O_2) with the ratio 10:1:1 respectively. 5 grams of citric acid monohydrate ($C_6H_8O_7$-H_2O) is also added to the solution. The sample is put into the etch solution for about one minute and then rinsed with water. This run is for control purposes. After this step the sample is again measured with DEKTAK profilometer. The difference with the first measurement gives us the etch rate which is generally about 200 nm/min. The etch depth should reach inside the p-type contact which is located at 1000 nm below the surface of the crystal in order to make the back contacts of our devices. Since the total thickness of the n-type contact and the pin diode part of the devices is less than one μm, the etch depth around 1.1-1.2 μm will serve well to reach the p-type contact. So etching takes around 270 seconds. After that the sample is checked again with DEKTAK profilometer to confirm the etch depth. Since there can be unintentional oxide layer on the sample, etch of the crystal may start later so that the last check is important. If the etch depth is sufficient, sample is successively soaked in acetone/methanol/isopropanol to remove the photoresist. The sample is finally rinsed with water and blown dry with N_2. As a final check the height of the mesa on the sample is measured with DEKTAK profilometer and a print-out is taken.

The mesa structures are ready at this stage. Now, we cover the surface with the passivation layer which may be SiO_2, Si_3N_4, Al_2O_3 or ODT. For SiO_x and SiN_x plasma enhanced chemical vapor deposition (PECVD) technique is used. In PECVD method thin films are deposited on a substrate by creation of plasma of the mixture of precursor gases with RF power. Freshly cleaned samples with mesa structures fabricated on it put into the process chamber. Chamber is vacuumed to get rid of the air and remnants of

gases from the previous processes. When the vacuum reaches down to the required value, precursor gases are allowed into the chamber. Precursor gases for SiO_x and SiN_x are N_2O/SiH_4 and NH_3/SiH_4, respectively. Parameters that affect the deposition rate are the RF power, chamber pressure, chamber temperature, flow rate of gases and deposition time.

Material	Flow Rate (sccm)	RF Power (Watts)	Temperature (°C)	Pressure (Torr)	Thickness (nm)
SiO_x	SiH_4(180) N_2O(250)	9	250	0.5	300
SiN_x	SiH_4(200) NH_3(20)	12	250	1	300

Table 3.1: PECVD recipes for SiO_x and SiN_x passivations.

In order to deposit a thin layer of Al_2O_3, atomic layer deposition method is used. ALD method is similar to chemical vapor deposition. The precursor gases are sent into a chamber in which they react and the outcome of the reaction is deposited on the surface of the sample. The difference of the ALD method with PECVD is the sequential nature of gas flow into the chamber. First, one of the precursor gases is let into the chamber. Then the system is left to wait before letting the other gas in, to ensure that the first gas is adsorbed on the sample surface. After the second gas is let into the chamber there is again a time delay before the second cycle of gas delivery. This delay time between the gas pulses makes sure that the there is enough reaction has time to occur. The outcome of the reaction is limited with the amount of the gases let into one cycle. This increases the thickness control ability. Each cycle defines an equal amount of film thickness. Therefore, the total number of cycles defines precisely the total thickness. The time delay between the cycles also increases the film uniformity. These reactions occur without plasma which is good for the crystal since plasma can cause microscopic damage to the crystal. For ALD Al_2O_3 we used a Cambridge Nanotech Savannah 100. The precursor gases which are water vapor (H_2O) and trimethylaluminum (TMA) are let into the chamber with pulses that are 0.015 s long. There was also 20 sccm N_2 flow during the whole process. The film growth is completed with 200 cycles. 200 cycles result in 20 nm film thickness of ALD deposited Al_2O_3 layer on sample.

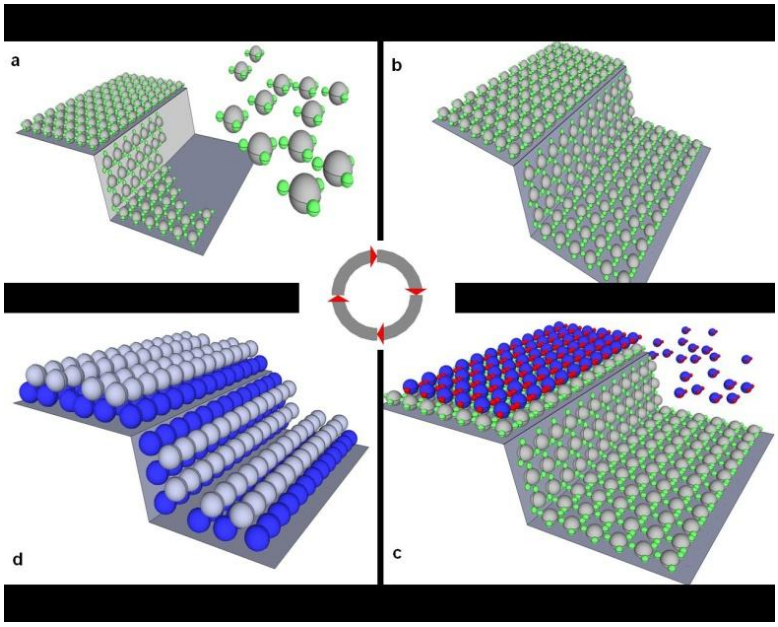

Figure 3.5: Visualization of ALD Al_2O_3 deposition on sample. (a) TMA molecules are sent into chamber and adsorb on the surface. (b) After some time surface is covered with TMA molecules and the chamber is purged. (c) As second pulse H_2O molecules sent into chamber. (d) At the end of the pulse Al2O3 molecules are formed on the surface and chamber is purged. Second cycle begins again with the TMA pulse

The application of SAM ODT onto the surface is done by dipping the sample into an ODT solution. First, samples are prepared for immersion into ODT solution. An HCl solution is prepared in isopropyl alcohol (3M) and samples are left in it for 1 min. followed by rinse in isopropanol. At this stage, samples are ready to immerse into 1mM ODT (Aldrich, %99) in ethanol solution. This step takes 48 hours and the solution should be kept at 60ºC. Finally, samples are first rinsed with ethanol and then iso and blow dry with N_2. Samples are now ODT passivated.

After the passivation layer is covered with the passivating layer the sample is again spun with photoresist with the same recipe as we do for etch mask lithography. The baking is again 55 seconds at 110 ºC. This time the UV expose is done with passivation mask, which masks only the sidewalls of the mesa. Then the sample is put into developer solution. The passivation layer around the mesa sidewalls is protected by the photoresist this time. Since we again apply an etch procedure the photoresist should be hardened. The sample is baked at 125ºC for 150 seconds. The etch acid is different in this case. HF solution in water (H_2O) and hydrofluoric acid (HF) in the ratio of 10:1, respectively is prepared. The sample should stay in the HF solution until the passivation layer is completely cleaned off from the unprotected surface. This takes 15-20 seconds. Then the sample is cleaned in acetone/methanol/iso, combination and rinsed in water and blown dry with N_2. Finally, metallization for ohmic contacts are made.

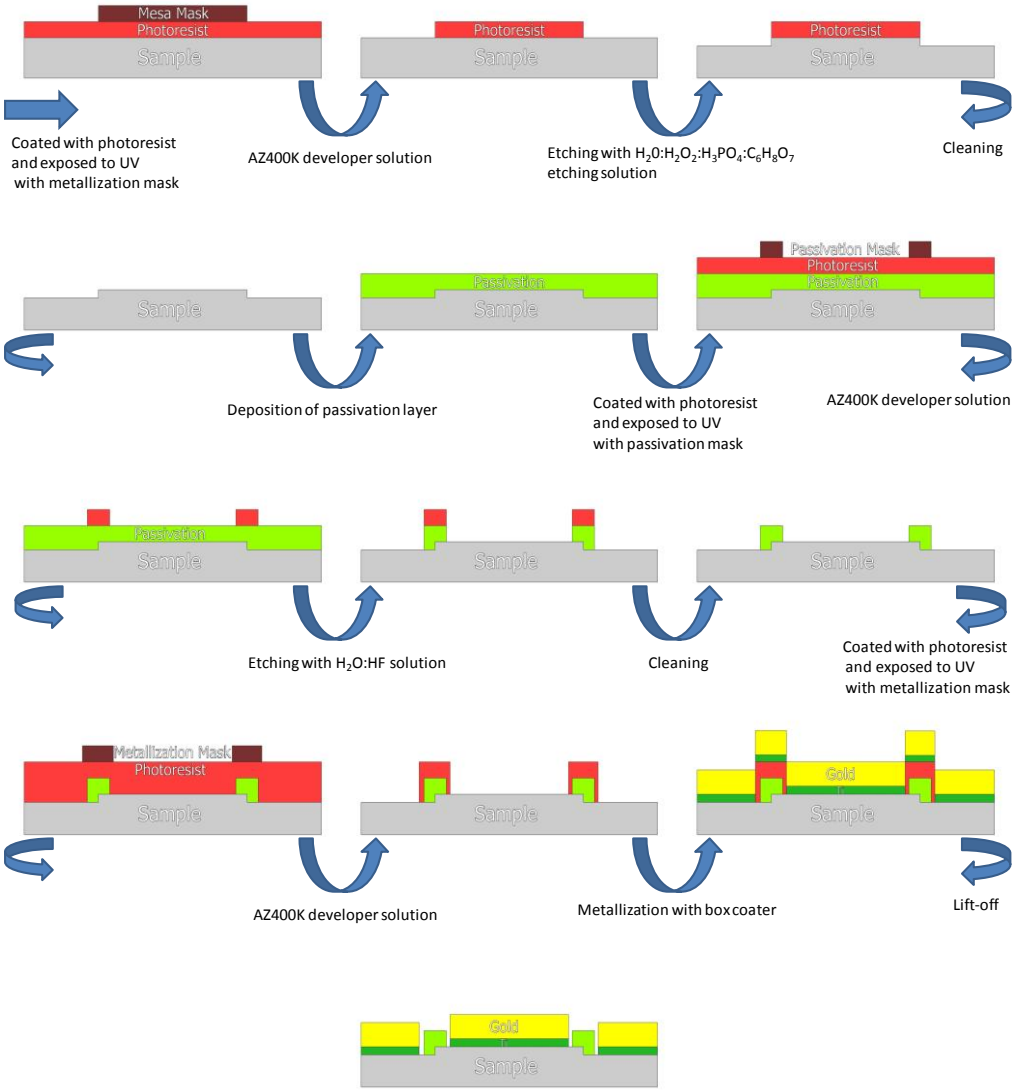

Figure 3.6: Schematic representation passivated InAs/GaSb type II superlattice IR photodetector fabrication.

In order to define the gold contacts the metallization mask is used. The sample is spun with photoresist, baked and exposed with the same recipe before. Then the sample is dipped into developer solution. This time only the passivated parts and the considerable part of the active region on top of the mesa are covered with photoresist. No post bake is used at this stage. Sample is ready to be Ti/Au evaporation.

Box coater is used for the Ti/Au metallization. The sample is placed inside the box coater. Then the system is pumped down for approximately 2.5 hours for the best vacuum of $5x10^{-6}$mbar. First a 5 nm thick Ti layer is sputtered onto the samples in order to get the gold to attach to the surface. Then, 200 nm gold is evaporated on top of

Ti. Contacts become ready after the lift-off process. Finally, the sample is placed into a warm acetone bath. After the lift-off, the sample is cleaned for the last time with acetone/methanol/iso, combination and rinsed in water and blown dry with N_2. The samples are mounted on a ceramic dual in-line package with 40 pins (cerdip40). After mounting, the contacts are bonded with the West Bond wedge bonder. With the bonding done sample is ready for measurement. There are two types of measurements that we performed on our samples. They are dark I-V measurements and responsivity measurements which will be described next.

Figure 3.7: West bond wedge bonder. The inset shows the needle and the gold thread.

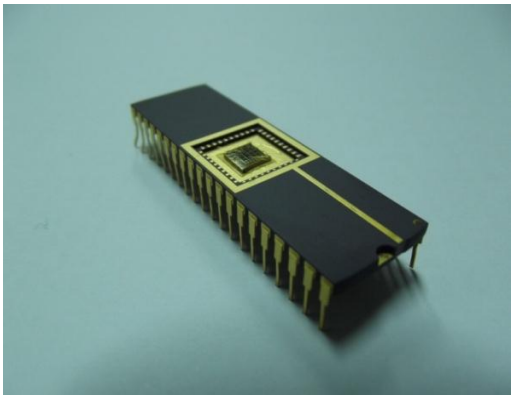

Figure 3.8: Ready to measure packaged sample.

3.3 I-V Measurement Setup

Since there is an internal current flowing inside the devices without any external stimuli which is called dark current, the signal that generates currents comparable to dark current cannot be separated from it and cannot be detected. The purpose of dark I-V measurements is to determine the lowest current that can be detected by the device in the absence of any IR photons. In order to block the externally generated current the

sample should be measured in total darkness. Since our detectors are able to detect the radiation from objects that is around room temperature, the background that the device sees should be at a much lower temperature then the room temperature. And also the device itself should be at a lower temperature since the band gap of our structure is so small that the self temperature of the device can create current as mentioned before.

Dark I-V measurements are taken with HP 4142B source measure unit. There are two different setups for measurements at 77K in liquid nitrogen and temperature dependent dark I-V measurements. In measurements in liquid nitrogen, the sample is mounted on a sample holder with 40 pin holders. A metal shield is wrapped around the holder. Then the metal shield with the sample is dipped into liquid nitrogen in a foam beaker. Every pin on the holder matches to a pin on the measurement box. In this measurement setup every device that is bonded to the cer-dip can be measured.

Temperature dependent dark I-V measurement setup consists of a cryostat instead of liquid nitrogen in a foam beaker. Our setup has a Cryo Industries cryostat with a Sumitomo CSW 71 water cooled He compressor, Cryo-con 32B temperature controller, Varian DS102 mechanical pump, Varian Turbo V70 turbo pump. The cer-dip is mounted on the cold finger of the cryostat with silver paste or silicon paste. There are two temperature sensors on the cryostat. One of them is on the tip of the cold finger. The other sensor is attached to the cer-dip with silver of silicone paste. Unfortunately the feed through that enables us to reach the detectors inside the cryostat has 8 wires. So we can only measure 7 devices at one time. The devices with the best performance are chosen according to the liquid nitrogen measurements and temperature dependent dark I-V measurement is performed on them. The feedthrough cables are fixed on the chosen pins. Then the cryostat is sealed and taken under vacuum in order to break the link between the cold finger and the casing of the cryostat which is also in contact with the atmosphere which is a huge heat bath. When the pressure reaches the required value which is around 10^{-6} torr, the compressor is started and the cold finger starts to get cold. The sensor at the tip of the cold finger reaches temperatures down to 4K. The sensor on the sample reaches temperatures down to 12K. After reaching the lowest temperature, the cold finger is heated up with a heater unit. When the temperature reaches a preset temperature, I-V measurement is done, with HP 4142B. During dark I-V measurements the fluctuation of the measurement temperature is less than 1K.

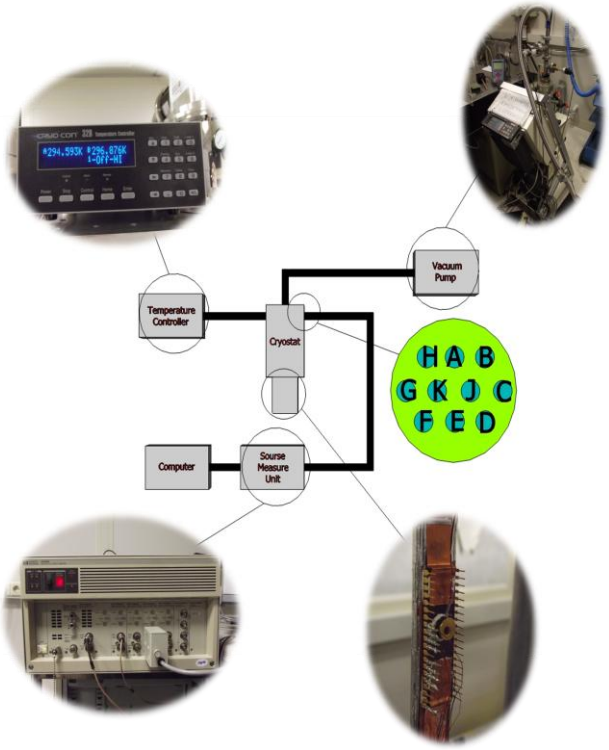

Figure 3.9: Schematic representation of temperature dependent dark current measurement setup.

3.4 Responsivity Measurements

The setup for responsivity measurement consists of a blackbody light source with a chopper mounted on the aperture of the source, a lock-in amplifier, a current preamplifier, a voltage preamplifier, a Fourier transform infrared spectrometer (FTIR) a temperature controller and a nitrogen cooled cryostat. The blackbody light source is turned on prior to the measurement since it takes time for the source to heat up. Temperature of the blackbody is set to 450K because the intensity distribution at that temperature covers the wavelengths that can be detected by our devices. The cer-dip is mounted on the cryostat cold finger with the help of silicon paste and the copper holders that not only hold the sample adjacent to the cold finger but also increases the heat transfer area between the package and the cold finger. Also temperature sensor is mounted on one of these copper holders. Feedthrough pins are connected to the package pins. Similar to the cryostat in the dark I-V measurement setup, the cryostat in the responsivity measurement setup has a limited number of feed through wires. So the pin configuration should be recorded to match the devices with the switchbox. It is also checked that if the device are in short contact with each other or the casing of the cryostat. If there is no electrical short the cryostat is closed and the system taken under vacuum for 1 hour and then liquid nitrogen is poured into the cryostat. In order to start

the measurement, temperature on the copper holder should reach 77K. First, we check how much current is generated due to the radiation from the blackbody. The chopper should be set to an odd frequency, like 13, that cannot interfere with environment. The window of the cryostat is brought in front of the blackbody light source aperture. Device that is designated to be measured is chosen from the switchbox. The current that is generated on the device first reaches to the current preamplifier and then to the lock-in amplifier that reads the photocurrent. This value is the peak responsivity value. In order to check how much of the light spectrum that is generated by the blackbody is detected by our device FTIR should be used. The output from our device is sent to the FTIR device through a voltage preamplifier. Our photodetector is used as the detector of the FTIR. By this way the responsivity is modified due to the spectrum that our photodetectors work. With the peak responsivity values, the spectrum from the FTIR gives us the responsivity of our devices.

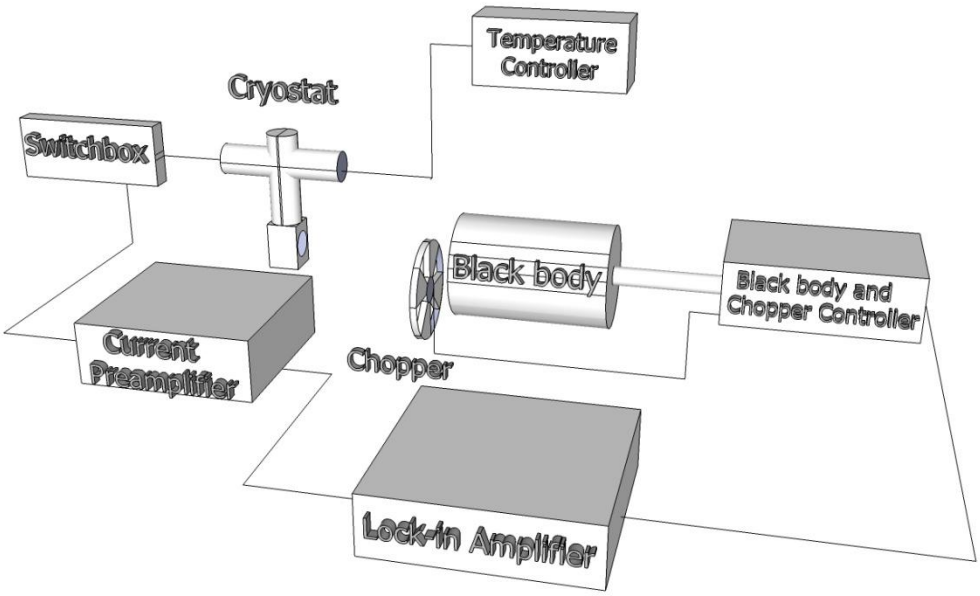

Figure 3.10: Peak responsivity measurement setup.

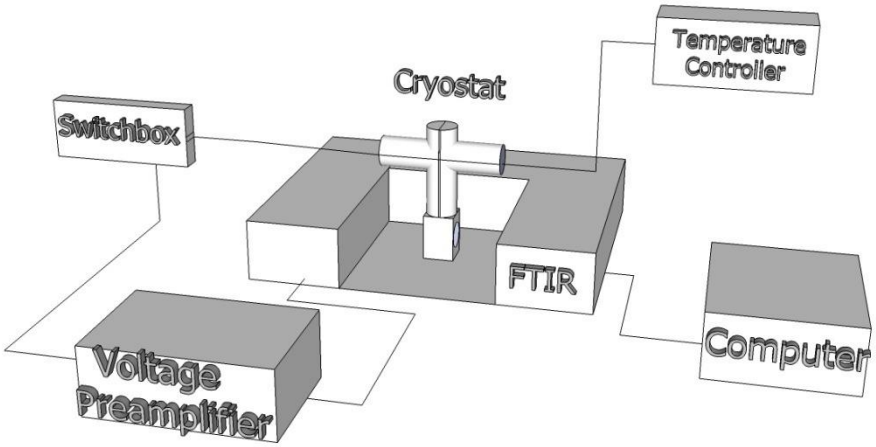

Figure 3.11: Cut-Off wavelength measurement setup.

3.5 Contact Resistance: Transmission Line Method

In order to measure the resistance of gold contacts on both n and p type surfaces we used transfer line matrix (TLM) method. In this method resistance values between gold pads on n or p type layer are measured for different distances between pads. Since the contacts can be taken as single points, the resistance for a point corresponds to resistance with zero distance. The resistance is plotted as a function of distance. The data from the measurements are linearly fitted. Linear fit equation can be modeled as;

$$R = 2R_c + (\rho/A)L \tag{3.1}$$

where R_c is contact resistance. Then the intercept of the fitted data with resistance axis gives contact resistance. The contact pad layout is given in the figure below.

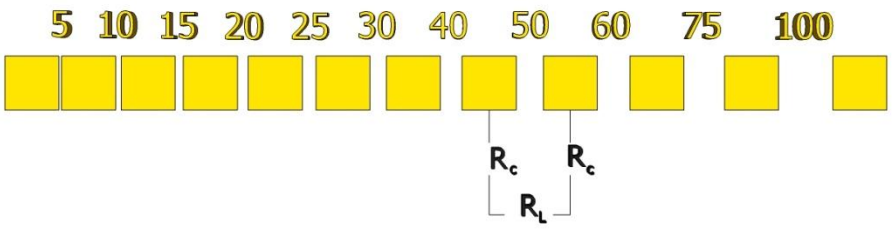

Figure 3.12: Layout for gold pads for TLM measurement.

Chapter 4

Measurements on Single Pixel Photodiodes

In this chapter, dark current measurements on InAs/GaSb type II superlattice photodiodes will be given. The constant temperature measurements for different sized mesa structures are done with a liquid nitrogen setup and the temperature dependent measurements are done in the closed cycle cryostat setup. Using the dark I-V measurements, zero bias resistance values (R_0A) are calculated. The spectral response and responsivity measurements are done with the black-body source and FTIR containing measurement setup. Quantum efficiency and Johnson-noise limited detectivity values are calculated from the spectral responsivity data. Each of the measurement sets for different passivation techniques are given. Additionally, transfer line method (TLM) measurements for contact resistance values are given.

4.1 Al_2O_3 Passivated Samples

This part of the thesis was published as "Atomic layer deposited Al_2O_3passivation of type II InAs/GaSb superlattice photodetectors_Ömer Salihoğlu, Abdullah Muti, Kutlu Kutluer, Tunay Tansel, Raşit Turan, Coşkun Kocabaş and Atilla Aydınlı, Journal of Applied Physics, 111, 074509 (2012)" Reproduced (or 'Reproduced in part) with permission from American Institute of Physics.

At 77 K detectors of all sizes (100x100 μm^2, 200x200 μm^2, 300x300 μm^2, 400x400 μm^2, 500x500 μm^2, 600x600 μm^2, 700x700 μm^2) are measured for both ALD Al_2O_3

passivated and unpassivated samples with the constant temperature liquid nitrogen measurement setup. In the figure below measurements for both sets of samples are given. After these measurements for 400x400 μm^2 sized passivated and unpassivated photodetectors are compared for both dark I-V and spectral response results.

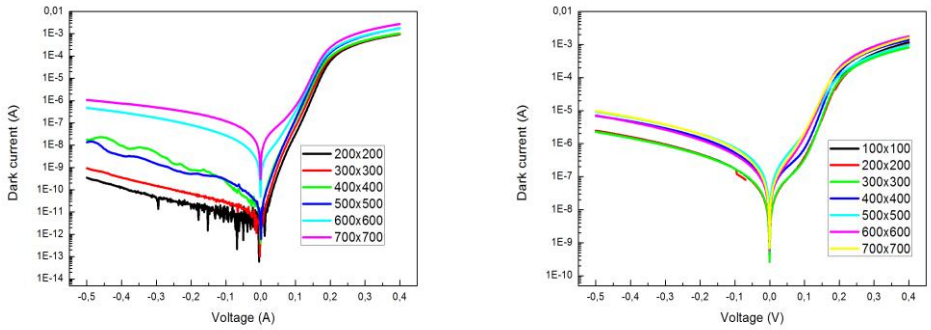

Figure 4.1: Comparison of dark currents of ALD Al_2O_3 passivated and unpassivated samples for different mesa sizes at 77K. Graph on the left belongs to passivated sample and graph on the right belongs to unpassivated sample.

Comparison of graphs in figure 4.1 clearly shows the lower dark currents measured for the passivated samples. In fact, the reverse biased dark current in small area passivated diodes display current levels beyond our measuring capacity and lead to pronounced noise, which we ignore in the rest of this thesis. The measurements at 77 K, in particular, for400x400 μm^2 sized photodetector result an almost two orders of magnitude decrease for Al_2O_3 passivated samples as compared to the unpassivated photodetector. Dark current density value for an unpassivated 400x400 μm^2 photodetector at -0.1 V bias voltage is 4.7×10^{-5} A/cm^2. Al_2O_3 passivation decreases this value to 6.6×10^{-7} A/cm^2. From the dark I-V measurements, R_0A values are deduced. The value for unpassivated detector, which is $1.6 \times 10^3 \Omega.cm^2$, is improved to be $3.7 \times 10^5 \Omega.cm^2$ with Al_2O_3 passivation. In figure 4.2 dark current densities for 400x400 μm^2 Al_2O_3 passivated and unpassivated samples are compared. Also the R_0A comparison is given in the same figure. Considering that IR photodetectors are typically used in near zero bias conditions, both the R_0A and dark current density values are among the best in the literature.

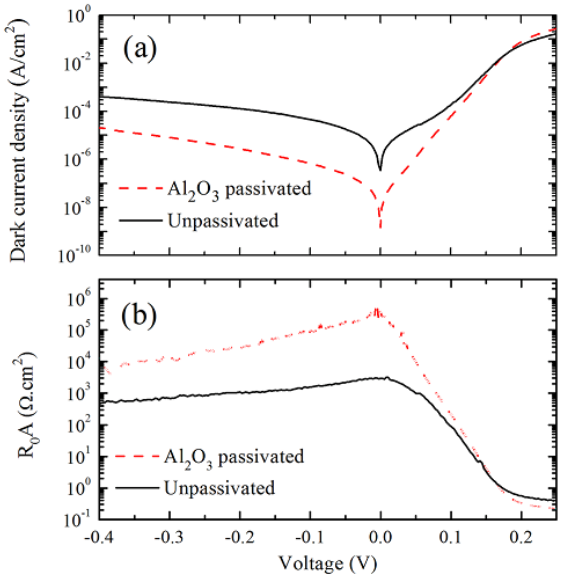

Figure 4.2: Dark current density comparison of passivated and unpassivated 400x400 μm^2 sized detectors (top graph). R0A value comparison for passivated and unpassivated samples (bottom graph).

Spectral responsivity measurements were performed on these samples and which gives the cut-off wavelength of the photodiodes as 5.1 μm for both Al_2O_3 passivated and unpassivated cases since cutoff wavelength is dependent on the crystal structure of superlattice and determined by the thicknesses of InAs and GaSb in each pair. Spectral responsivity rises rapidly below 5.1 μm and reaches to a maximum and finally saturates towards shorter wavelengths.

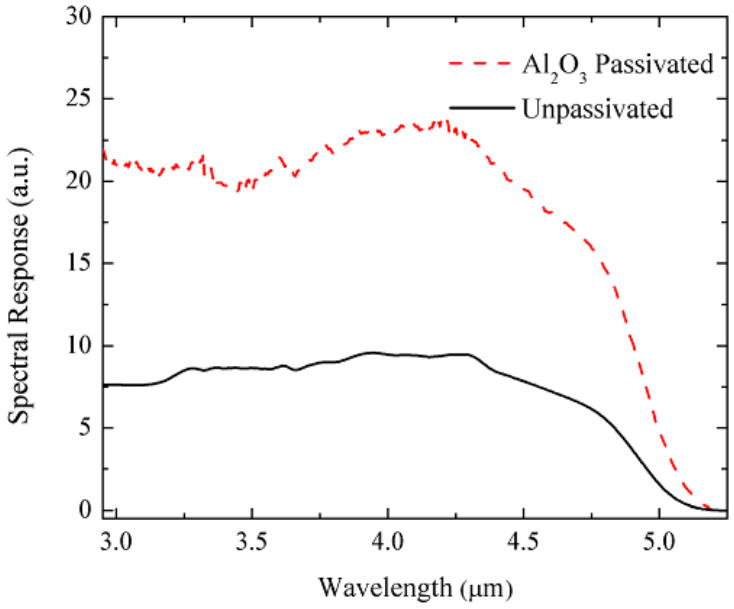

Figure 4.3: Spectral response measurement results for passivated and unpassivated samples.

In figure4.4 we show the measured responsivity as a function of applied reverse bias for 4 μm. We also display the calculated detectivity on the second y-axis. Zero bias responsivity is found to be 1.33A/W for Al_2O_3 passivated detector at 77 K and 4 μm wavelength. The Johnson-limited detectivity is calculated as 1.9×10^{13} Jones at zero bias at 77 K and 4 μm wavelength.

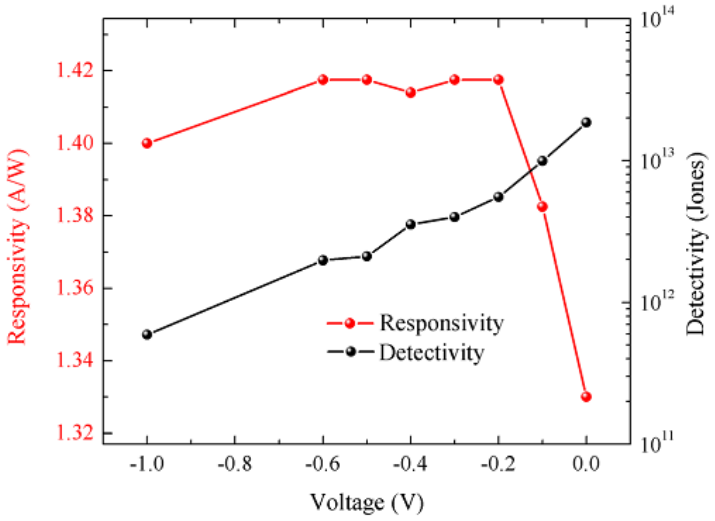

Figure 4.4: Responsivity and detectivity results of 400x400 μm sized passivated sample at 77K and 4 μm wavelength.

The temperature dependent dark I-V is also measured. Temperatures for these measurements are set as 30K, 40 K, 50K, 60K, 77K, 100K, 150K, 200K, and 245K. The density of measurements as a function of temperature for different regions is chosen with a 1000/T plot in mind. Since for higher temperatures the 1000/T values pile up together, there is no need to make measurements at temperatures close to each other in this temperature region. As mentioned earlier we have seven different mesa sizes on our chips. The temperature dependent dark I-V measurements are done for all these seven mesa sizes. Temperature dependent dark current density measurements for both ALD Al_2O_3 passivated and unpassivated samples for selected mesa sizes are given in the figure 4.5 below. Graphs on the left hand side shows data from the passivated samples and graphs on the right belongs to unpassivated samples. Mesas with sizes of 600x600 μm^2, 400x400 μm^2, 300x300 μm^2 and 200x200 μm^2 are shown from top to bottom, respectively, figure 4.5. For temperatures at and below 100K at least one order of magnitude decrease for passivated samples are seen from the graphs. Temperatures at and above 150K, the dark current density is very close to each other for passivated and unpassivated samples. This implies that the dark current mechanism that we are suppressing by ALD Al_2O_3 passivation is effective mostly at temperatures below 150K.

The I-V curves of unpassivated samples are smooth functions of both temperature and bias voltage with the exception of the smallest diodes at the lowest temperature. We find that all I-V curves at and below 100 K cluster around similar values while at higher temperature the dark current densities increase. The passivated samples have similar behavior with the significant exception that the dark current densities are much lower as in figure 4.5. In addition, dark current densities for passivated samples show excessive noise at low temperature and small diodes due to the limitations of the measurement system.

In order to check the temperature dependency for a selected bias voltage, dark current density values at this voltage are plotted against 1000/T. We choose -0.1V bias voltage for this purpose.

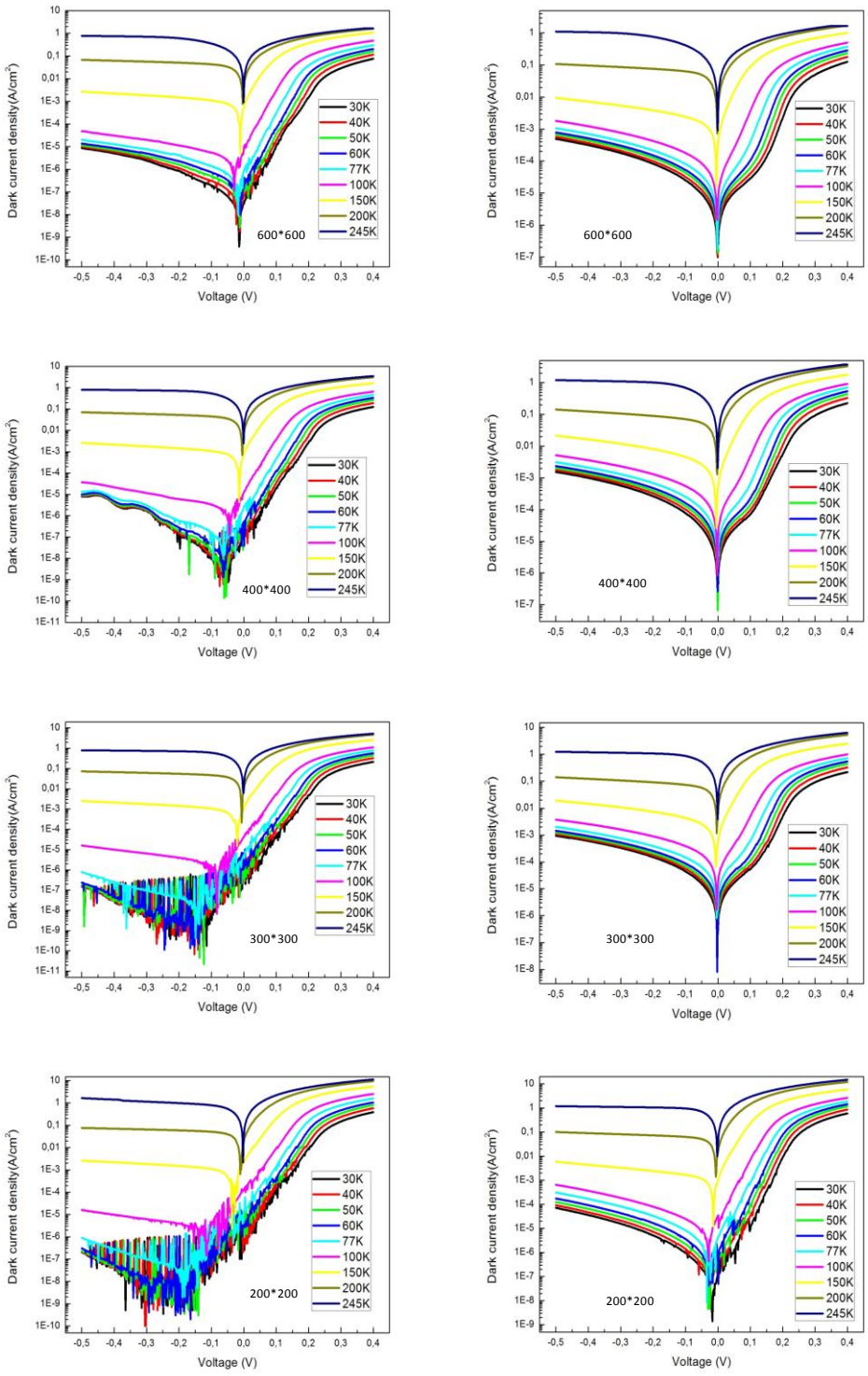

Figure 4.5: Temperature dependent dark current density comparison of ALD Al2O3 passivated (left block) and unpassivated sample (right block) for 600x600 μm^2, 400x400 μm^2, 300x300 μm^2, 200x200 μm^2 sized photodiodes.

The dark current density dependence on temperature shows two different distinct regions, as can be seen in figure 4.6. The differences in the slope of the curve of dark current density vs. 1000/T indicates that there are two different and distinct dark current

mechanisms for these different temperature regions. As can be seen from the figure, the curve for ALD Al_2O_3 passivated samples starts to converge to the curves of unpassivated samples above 100K and merges to each other at approximately 150 K. Suppression of surface leakage mechanisms less than 150K can clearly be seen. Also similar values of dark current density above 150K indicates that dark currents above 150 K cannot be totally suppressed by our passivation method, Mechanisms that contribute to dark current above 150 K acts similarly on both passivated and unpassivated devices. As was mentioned in Chapter 2, other dark current mechanisms related with the device itself are diffusion current and generation-recombination current. We can, therefore, conclude the dominant dark current mechanisms above 150K are diffusion current and G-R current. Their individual contributions to total dark current density may vary with temperature.

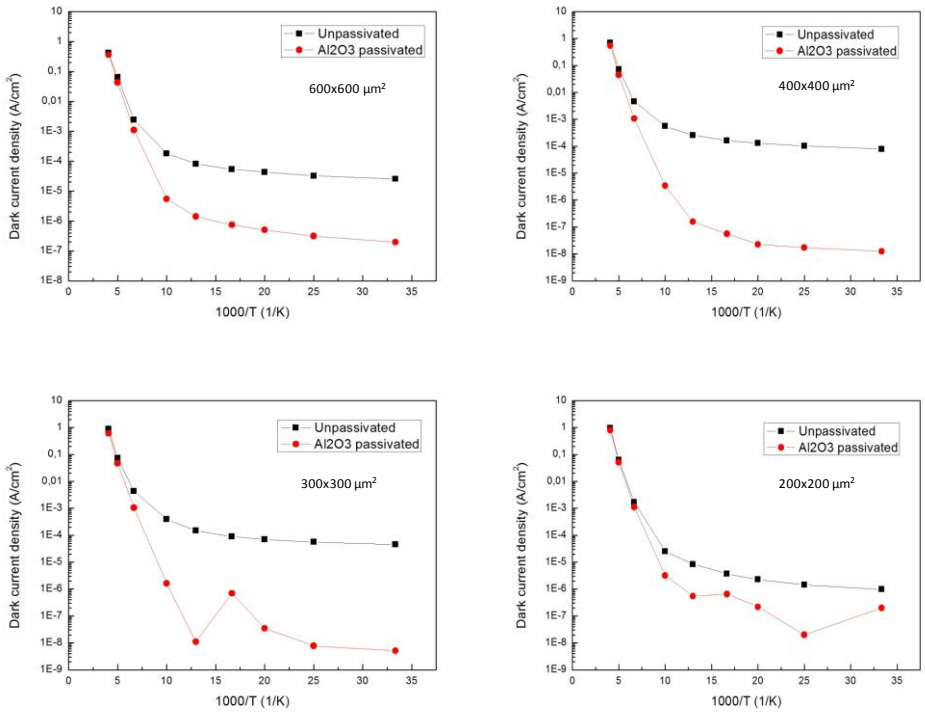

Figure 4.6: Comparison of temperature dependent dark current density values of ALD Al_2O_3 passivated and unpassivated samples for 600x600 μm^2, 400x400 μm^2, 300x300 μm^2,200x200 μm^2 sized photodiodes at -0,1 V.

Finally, dark current density of a 400x400 μm^2 diode with I-V data at many more temperatures is shown below. The difference between unpassivated and passivated samples is clearly seen for temperatures below 150 K. Below a more sensitive temperature dependent dark current density for -0.1V bias measurement result is given for 400x400 μm^2 for both passivated and unpassivated diodes.

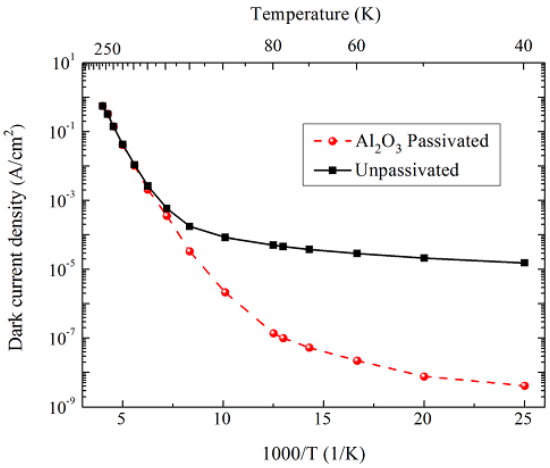

Figure 4.7: Temperature dependent dark current density values of ALD Al_2O_3 passivated and unpassivated 400x400 μm^2 sized photodiodes at -0.1V.

4.2 ODT SAM Passivated Samples

This chapter was published as "Skin-like self assembled monolayers on InAs/GaSb superlattice photodetectors_Ömer Salihoğlu, Abdullah Muti, Kutlu Kutluer, Tunay Tansel, Raşit Turan and Atilla Aydınlı, Journal of Physics D: Applied Physics, 45, 365102 (2012)" Reproduced" (or 'Reproduced in part') with permission from IOP Publishing Ltd.

Same measurement pattern is followed for the ODT SAM passivated samples. However, the mask design is different from the mask used in the ALD Al_2O_3 passivation case. There are only 3 different mesa sizes for ODT SAM passivated samples (400x400 μm^2, 500x500 μm^2, 600x600 μm^2). At 77 K ODT SAM passivated 400x400 μm^2 sized photodiodes shows two orders of magnitude decrease in dark current density as compared to the unpassivated photodiodes, given in figure 4.8. At 77 K and under -0.1 V bias, dark current density value changes from 1.1×10^{-5} A/cm^2 to 3.1×10^{-7} A/cm^2 for unpassivated and ODT SAM passivated samples respectively. According to these measurements R_0A value for unpassivated photodiode improves from $1.8\times10^4\Omega.cm^2$ to $3.2\times10^5\ \Omega.cm^2$ for ODT SAM passivated photodiodes.

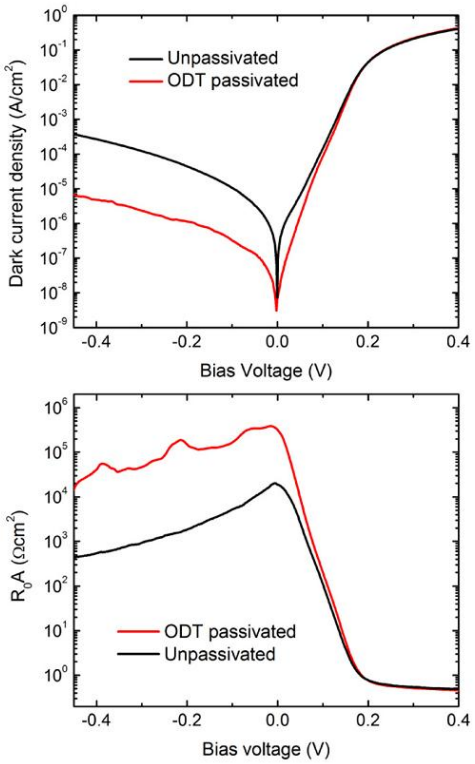

Figure 4.8: Dark current density comparison between ODT SAM passivated and unpassivated 400x400 μm^2 sized devices at 77K (top graph). R_0A value comparison for same devices (bottom graph).

The spectral response for the passivated sample has been measured and gives us a cut-off wavelength is determined to be 5.1 μm as can be seen from figure 4.9. For 77 K and 4 μm zero bias responsivity of ODT SAM passivated sample is 1.04 A/W and the peak detectivity is found as 2.15×10^{13} Jones. The quantum efficiency of this sample at 4 μm is higher than 30%.

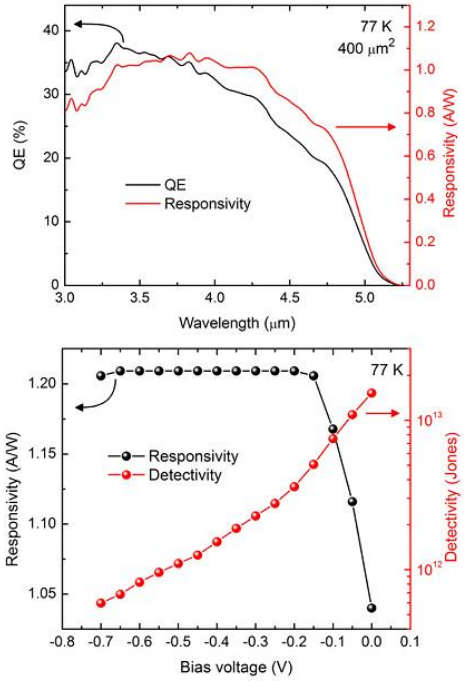

Figure 4.9: Quantum efficiency, responsivity and detectivity results for 400x400 μm^2sized device at 77K and 4 μm.

Temperature dependent measurements are done for both ODT SAM passivated and unpassivated 400x400 μm^2 sized diodes. In the following, figure 4.10, temperature dependent dark I-V curves are given for passivated and unpassivated photodiode. The general behavior of the I-V curves of both passivated and unpassivated samples are similar to the case of Al_2O_3passivation At and below 100 K the I-V curves cluster together and increase above 100 K. For thiol passivated samples at low temperature and relatively large bias of 0.25V, we observe a bump which we suspect is due to tunneling. This point will be further studied.

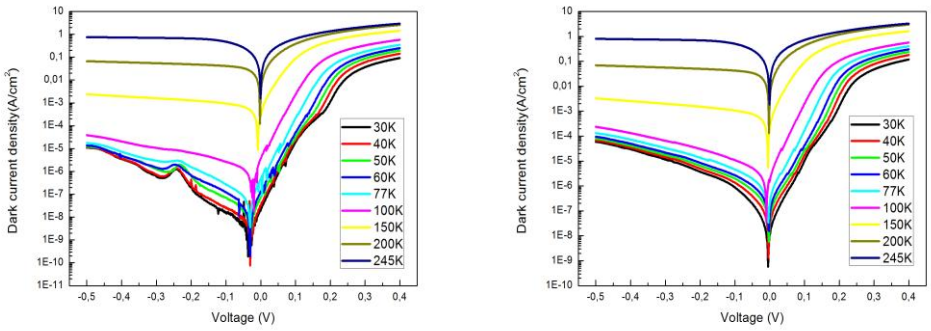

Figure 4.10: Dark current density comparison of ODT SAM passivated (left graph) and unpassivated (right graph) samples at 77K.

The ODT is a sulphur based passivation technique and the problem with the sulphur passivation has been the degradation of the performance of the passivation over time.

We, therefore, checked to see if the dark I-V measurements show degradation in performance over time. We performed temperature dependent I-V measurements for a 65 day time period. The measurements are taken 11, 20, 33 and 65 days after the first measurement. Performance of the passivation seems not to be affected by time. Dark current values for -0.1 V bias for a temperature range show that affect of passivation does not wear-off for 65 days, given in figure 4.11.

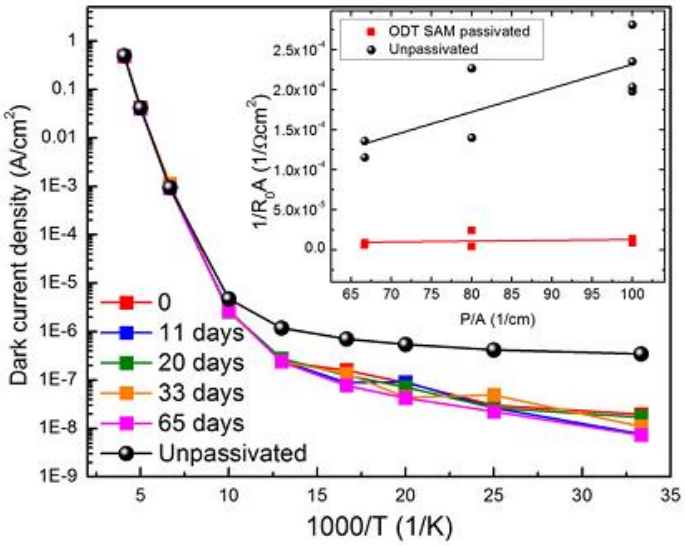

Figure 4.11: Degradation control on performance of ODT SAM passivation through time delayed temperature dependent dark current density measurements for 400x400 μm^2at -0.1V. Inset shows the relation between perimeter to area ratio and inverse zero bias area resistance.

4.3 Comparison with Other Passivation Methods

The typical passivation methods in the industry are SiO_2 and Si_3N_4. This is especially true of SiO_2. We, therefore, used these passivation methods on the same pin structure that we used for ALD Al_2O_3 passivation, for comparison. Temperature dependent dark current density graphs for both SiO_x and SiN_x passivated samples for all sizes are given in the figure below, Fig. 701. The graphs show mesa sizes for 600x600 μm^2, 400x400 μm^2, 300x300 μm^2, 200x200 μm^2 from top to bottom respectively. In general, SiO_x passivation gives better results than the SiN_x passivation as can be seen in figure 4.12.

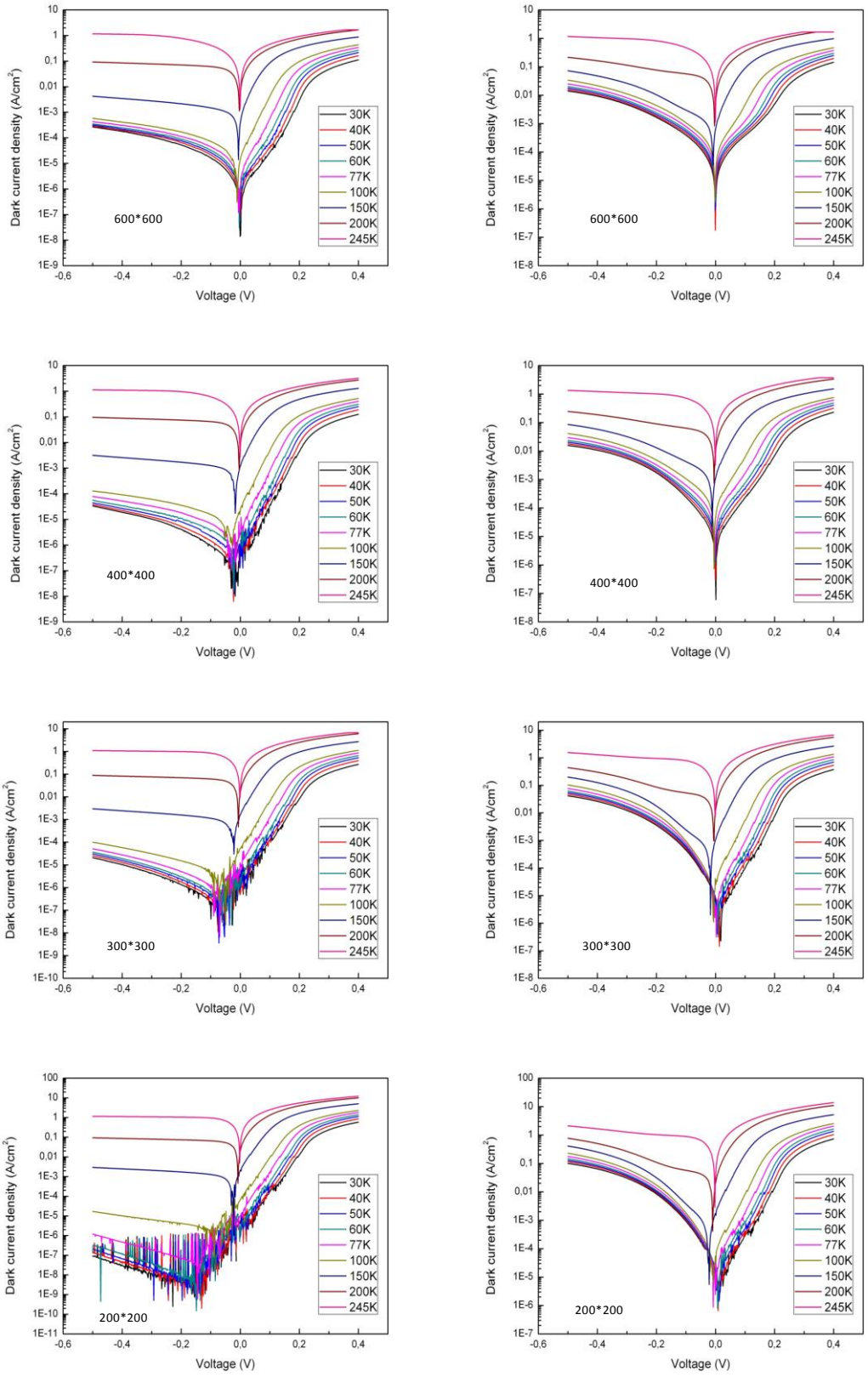

Figure 4.12: Temperature dependent dark current density comparison between SiO_x passivated (left block) and SiN_x passivated (right block) 600x600 μm^2, 400x400 μm^2, 300x300 μm^2, 200x200 μm^2 mesa sized detectors.

In order to make an overall comparison, dark current density values for -0.1V bias, for all device sizes mentioned above and for all types of passivation techniques, are plotted as a function of inverse temperature, in figure 4.13.

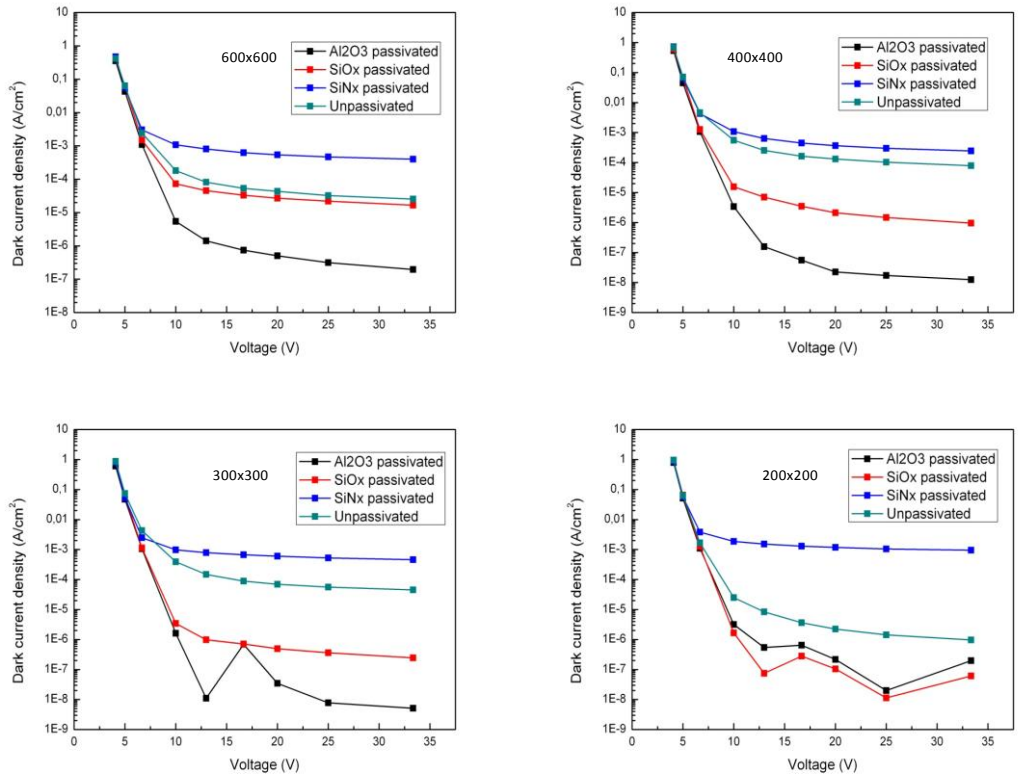

Figure 4.13: Temperature dependent dark current density comparison for ALD A_2O_3 passivated, SiO_x passivated, SiN_x passivated and unpassivated 600x600 μm^2, 400x400 μm^2 , 300x300 μm^2, 200x200 μm^2sized detectors at -0.1V.

It can be seen from the graphs that the SiN_x passivated samples result in the highest dark current density values when compared with the unpassivated samples. We feel that SiN_x and the deposition techniques used seems to generate extra surface states on the mesa sidewalls which act as new current channels and lead to the increase in dark current. While the performance of SiO_2 passivation is very good, it is obvious that ALD Al_2O_3 passivated samples shows even better performance than the SiO_2 passivated samples. We conclude that the temperature depend behavior of all passivation techniques are similar albeit of different magnitudes. It can again be understood that below 150K the surface based dark current mechanism are dominant. Bulk based dark current mechanism starts to be effective above 150K.

4.4 TLM Measurements

A critical step in the fabrication of semiconductor devices is the electrical contact of the devices with outside world. The aim is to generate a junction with the lowest possible resistance as well as linear characteristics in order not to complicate the analysis and derive the devices with appropriate voltage. To investigate the resistance of both p and n type contact layers TLM method is typically used. Selected results are given below in figure 4.14.

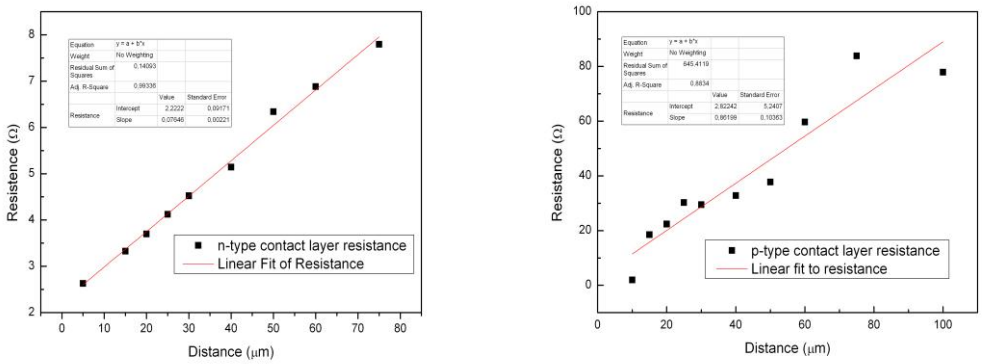

Figure 4.14: TLM measurement results for n-type contact layer (left graph) and p-type layer (right graph).

From the two figures above the contact resistance of both p and n type surfaces are found by linear fitting. The resistance for n-type layer is 2,22Ω and the resistance for p-type layer is 2,8 Ω.

Chapter 5

Conclusions

In this thesis we are focused on alternative passivation layers in order to suppress dark current that is caused by the surface states. Conventional methods for this purpose are dielectric material deposition, application of chalcogenide materials to the surface, polyimide deposition, and epitaxial overgrowth of a dielectric on the surface. Each of these methods has their own advantages and disadvantages. The alternative methods that we are proposing are ALD Al_2O_3 and ODT SAM passivations. Al_2O_3 is a dielectric so that we made comparison of these materials with other dielectric materials like SiO_x and SiN_x. ODT SAM passivation depends on the working principle of sulphur passivation. Therefore, the ODT SAM passivation is checked if it shows same drawbacks with the sulphur passivation.

The comparisons made through liquid temperature measurements with liquid nitrogen setup, temperature dependent measurement setup and optical measurement setup. ALD Al_2O_3 passivated samples are also compared due to different sized devices. Liquid nitrogen measurements for both passivated and unpassivated samples at are given for all sizes. Temperature dependent measurements are given for selected mesa sizes. Additionally, in order to understand behavior of different dark current mechanisms on different temperature ranges inverse temperature versus dark current plots are generated for -0.1V bias. Clearly a change of mechanism for dark current is seen. For temperatures below 150 K it is observed that our passivation layer is effective in suppression of dark current. This states that the surface states that we passivated are effective in total dark current for temperatures below 150K.

In order to compare ALD Al_2O_3 passivation with other passivations based dielectric deposition SiO_x and SiN_x passivated samples are used. Temperature dependent dark current densities for all sized devices are compared for SiO_x and SiN_x passivation. SiO_x result show better dark current suppression than SiN_x passivation. For further investigation inverse temperature curves for ALD Al_2O_3 passivated, SiO_x passivated, SiN_x passivated and unpassivated samples are compared. Although the SiO_x passivation shows a good performance for dark current suppression ALD Al_2O_3 proves to be a better method. SiN_x passivation, on the other hand, gives increase in dark current even compared to unpassivated samples, which may be due to generation of new surface states through deposition of SiN_x.

For ODT SAM passivated samples again dark current suppression is compared with liquid nitrogen cooled measurements. The current suppression is clearly seen between the passivated and unpassivated samples. Temperature dependent measurements for ODT SAM passivated and unpassivated sample showed similar behavior with the ALD Al_2O_3 passivated samples. Dark current suppression is obvious. And also the temperature range for the surface states to be effective on total dark current seems to be same with Al_2O_3 passivation.

Besides the measurement pattern similar to ALD AL_2O_3 passivated sample ODT SAM passivated samples are also checked for performance degradation over time. Inverse temperature versus dark current curves for -0.1V bias does not show a sign of degradation over a 65 days time period. This can be a solution for the performance degradation seen for sulphur passivation.

Both dark current density and spectral response measurements are done on the InAs/GaSb type II superlattice single pixel infrared detectors for ALD Al_2O_3 passivated samples, ODT SAM passivated samples and their unpassivated control samples for a selected 400x400 μm^2 sized device is given below. According to the measurements at 77 K and -0.1V bias the dark current density for 400x400 μm^2 sized photodetectors decreases from $4.7\times10^{-5}A/cm^2$ to 6.6×10^{-7} A/cm^2 for ALD Al_2O_3 passivated samples as compared to the unpassivated photodiodes. The samples with ALD Al_2O_3 passivated samples also shows responsivity value for 77K and 4 μm wavelength as 1.33A/W for zero biasing. For the same measurement conditions 400x400 μm^2 sized photodetectors with ODT SAM passivation has a dark current density of 3.1×10^{-7} A/cm^2 instead of 4.7×10^{-5} A/cm^2 for unpassivated samples. The responsivity measured for ODT SAM passivated 400x400 μm^2 passivated samples for again 77 K and 4 μm wavelength is 1.04A/W for zero biasing. Additionally the aging of the ODT SAM passivated samples is investigated. The measurements at 11^{th}, 20^{th}, 33^{rd}, 65^{th}, days results similar dark current density values at -0.1V biasing which shows that the aging effect is suppressed for sulphur passivation by the help of ODT structure.

	Diode Structure	Cut-off Wavelength (μm)	Dark Current Density (A/cm^2)	R_0A (Ωcm^2)
Plis et al. (2007) [28]	p-i-n	4.2 (82K) 5 (240K)	$5x10^{-7}$ (-0.1V, 82K) 0.18 (-0.1V, 82K)	$1x10^{-5}$ (82K) 0.24 (240K)
Kim et al. (2008) [52]	nBn	4.2 (77K)	$1x10^{-7}$ (-0.7V,77K)	
Bishop et. al. (2008) [22]	nBn	4.8 (250K)	$2.3x10^{-6}$ (-0.1V,77K) $3.1x10^{-4}$ (-0.1V,77K)	
Cervera et al. [12]	p-i-n	4.55 (77K)	$6.2x10^{-8}$ (-0.05V,77K)	$1x10^{6}$ (77K)
ALD Al_2O_3	p-i-n	5.1 (77K)	$1x10^{-7}$ (-0.1V,77K)	$3.7x10^{5}$ (77K)
ODT SAM	p-i-n	5.1 (77K)	$2.7x10^{-7}$ (-0.1V,77K)	$3.2x10^{5}$ (77K)

Table 4.1: Comparison of ALD Al_2O_3 and ODT SAM passivation with state-of-the-art photodiodes

As can be seen in table 4.1 the results are comparable with state-of-the-art photodiodes. The best result is 6.2x10-8 A/cm2 by Cervera et al. Dark current density value is given for -50mV bias. Dark current density values for 400x400 μm^2 sized diode with ALD Al_2O_3 passivation and ODT SAM passivation for -50mV bias are $1x10^{-7}$ A/cm^2 and $7.8x10^{-8}$ A/cm^2 respectively.

The TLM measurements that we made show that the contact resistance for both p and n type layer is around 2 Ω. This resistance values are not at a level to be taken as a complication for our device model.

The passivation that we are proposing proved to be showing better performance than their inspiration methods which are SiO_x and SiN_x passivations for ALD Al_2O_3 and sulphur passivation for ODT SAM passivation. Concluding by the measurements on both ALD Al_2O_3 passivated, ODT SAM passivated and their unpassivated control samples these two passivation technique that we are proposing fulfills the requirements that are expected from a passivation layer. They both generate a protective layer on the mesa side walls, eliminate the surface states which are in our case are the native oxides of the materials that our superlattice structures been made of and ultimately decreases the dark current density.

Bibliography

[1] Sze, S.M., *Citation Classic - Physics of Semiconductor-Devices.* Current Contents/Engineering Technology & Applied Sciences, 1982(27): p. 674.

[2] Nguyen, B.M., et al., *Demonstration of midinfrared type-II InAs/GaSb superlattice photodiodes grown on GaAs substrate.* Applied Physics Letters, 2009. **94**(22).

[3] Grein, C.H., P.M. Young, and H. Ehrenreich, *Minority-Carrier Lifetimes in Ideal Ingasb/Inas Superlattices.* Applied Physics Letters, 1992. **61**(24): p. 2905-2907.

[4] Youngdale, E.R., et al., *Auger Lifetime Enhancement in InAs-Ga(1-X)In(x)Sb Superlattices.* Applied Physics Letters, 1994. **64**(23): p. 3160-3162.

[5] Smith, D.L. and C. Mailhiot, *Proposal for Strained Type-II Superlattice Infrared Detectors.* Journal of Applied Physics, 1987. **62**(6): p. 2545-2548.

[6] Wei, Y.J. and M. Razeghi, *Modeling of type-II InAs/GaSb superlattices using an empirical tight-binding method and interface engineering.* Physical Review B, 2004. **69**(8).

[7] Walther, M., et al., *Growth of InAs/GaSb short-period superlattices for high-resolution mid-wavelength infrared focal plane array detectors.* Journal of Crystal Growth, 2005. **278**(1-4): p. 156-161.

[8] Wei, Y.J., et al., *Uncooled operation of type-II InAs/GaSb superlattice photodiodes in the midwavelength infrared range.* Applied Physics Letters, 2005. **86**(23).

[9] Wei, Y., et al., *High-performance type-II InAs/GaSb superlattice photodiodes with cutoff wavelength around 7 μm.* Applied Physics Letters, 2005. **86**(9).

[10] Sullivan, G.J., et al., *Molecular beam epitaxy growth of high quantum efficiency InAs/GaSb superlattice detectors.* Journal of Vacuum Science & Technology B, 2005. **23**(3): p. 1144-1148.

[11] Nguyen, B.M., et al., *Very high quantum efficiency in type-II InAs/GaSb superlattice photodiode with cutoff of 12 μm.* Applied Physics Letters, 2007. **90**(23).

[12] Cervera, C., et al., *Dark Current and Noise Measurements of an InAs/GaSb Superlattice Photodiode Operating in the Midwave Infrared Domain.* Journal of Electronic Materials, 2012. **41**(10): p. 2714-2718.

[13] Meyer, J.R., et al., *Type-II Quantum-Well Lasers for the Midwavelength Infrared.* Applied Physics Letters, 1995. **67**(6): p. 757-759.

[14] Aifer, E.H., et al., *Dual band LWIR/VLWIR type-II superlattice photodiodes.* Infrared Technology and Applications XXXI, Pts 1 and 2, 2005. **5783**: p. 112-122.
[15] Aifer, E.H., et al., *W-structured type-II superlattice long-wave infrared photodiodes with high quantum efficiency.* Applied Physics Letters, 2006. **89**(5).
[16] Vurgaftman, I., et al., *Graded band gap for dark-current suppression in long-wave infrared W-structured type-II superlattice photodiodes.* Applied Physics Letters, 2006. **89**(12).
[17] Nguyen, B.M., et al., *Type-II "M" structure photodiodes: An alternative material design for mid-wave to long wavelength infrared regimes - art. no. 64790S.* Quantum Sensing and Nanophotonic Devices IV, 2007. **6479**: p. S4790-S4790.
[18] Nguyen, B.M., et al., *Dark current suppression in type IIInAs/GaSb superlattice long wavelength infrared photodiodes with M-structure barrier.* Applied Physics Letters, 2007. **91**(16).
[19] Hoffman, D., et al., *The effect of doping the M-barrier in very long-wave type-II InAs/GaSb heterodiodes.* Applied Physics Letters, 2008. **93**(3).
[20] Maimon, S. and G.W. Wicks, *nBn detector, an infrared detector with reduced dark current and higher operating temperature.* Applied Physics Letters, 2006. **89**(15).
[21] Rodriguez, J.B., et al., *nBn structure based on InAs/GaSb type-II strained layer superlattices.* Applied Physics Letters, 2007. **91**(4).
[22] Bishop, G., et al., *nBn detectors based on InAs/GaSb type-II strain layer superlattice.* Journal of Vacuum Science & Technology B, 2008. **26**(3): p. 1145-1148.
[23] Plis, E., et al., *High performance dual-band InAs/GaSb SLS detectors with nBn and pBp architectures.* Infrared Technology and Applications Xxxvii, 2011. **8012**.
[24] Altarelli, M., *Electronic-Structure and Semiconductor-Semimetal Transition in Inas-Gasb Super-Lattices.* Physical Review B, 1983. **28**(2): p. 842-845.
[25] Wei, Y.J., et al., *Type IIInAs/GaSb superlattice photovoltaic detectors with cutoff wavelength approaching 32 μm.* Applied Physics Letters, 2002. **81**(19): p. 3675-3677.
[26] Hood, A., et al., *On the performance and surface passivation of type IIInAs/GaSb superlattice photodiodes for the very-long-wavelength infrared.* Applied Physics Letters, 2005. **87**(15).
[27] Rehm, R., et al., *InAs/GaSb superlattice focal plane arrays for high-resolution thermal imaging.* Opto-Electronics Review, 2006. **14**(1): p. 19-24.
[28] Plis, E., et al., *Type II InAs/GaSb strain layer superlattice detectors with p-on-n polarity.* Applied Physics Letters, 2007. **91**(13).
[29] Forrest, S.R., *Performance of Inxga1-Xasyp1-Y Photo-Diodes with Dark Current Limited by Diffusion, Generation Recombination, and Tunneling.* Ieee Journal of Quantum Electronics, 1981. **17**(2): p. 217-226.
[30] Hopkins, F.K. and J.T. Boyd, *Dark Current Analysis of Insb Photodiodes.* Infrared Physics, 1984. **24**(4): p. 391-395.
[31] Nguyen, J., et al., *Dark current analysis of InAs/GaSb superlattices at low temperatures.* Infrared Physics & Technology, 2009. **52**(6): p. 317-321.

[32] Yang, Q.K., et al., *Investigation of trap-assisted tunneling current in InAs/(GaIn)Sb superlattice long-wavelength photodiodes.* Applied Physics Letters, 2002. **81**(25): p. 4757-4759.
[33] Bessolov, V.N. and M.V. Lebedev, *Chalcogenide passivation of III-V semiconductor surfaces.* Semiconductors, 1998. **32**(11): p. 1141-1156.
[34] Plis, E., et al., *Electrochemical sulphur passivation of InAs/GaSb strain layer superlattice detectors.* Electronics Letters, 2006. **42**(21): p. 1248-1249.
[35] Hood, A., et al., *Near bulk-limited R(0)A of long-wavelength infrared type-II InAs/GaSb superlattice photodiodes with polyimide surface passivation.* Applied Physics Letters, 2007. **90**(23).
[36] Rehm, R., et al., *Passivation of InAsA/(GaIn)Sb short-period superiattice photodiodes with 10 μm cutoff wavelength by epitaxial overgrowth with Al(x)Ga(1-x)As(y)Sb(1-y).* Applied Physics Letters, 2005. **86**(17).
[37] Gin, A., et al., *Passivation of type IIInAs/GaSb superlattice photodiodes.* Thin Solid Films, 2004. **447**: p. 489-492.
[38] Plis, E., et al., *Passivation of long-wave infrared InAs/GaSb strained layer superlattice detectors.* Infrared Physics & Technology, 2011. **54**(3): p. 252-257.
[39] Li, J.V., et al., *Passivation of AlGaAsSb/InGaAsSb/GaSb photodiodes using aqueous (NH4)(2)S solution and polyimide encapsulation.* Journal of Applied Physics, 2005. **97**(10).
[40] Hoffmann, J., et al., *Advantages and disadvantages of sulfur passivation of InAs/GaSb superlattice waveguide photodiodes.* Semiconductor Science and Technology, 2009. **24**(6).
[41] Hollinger, G., R. Skheytakabbani, and M. Gendry, *Oxides on GaAs and InAs Surfaces - an X-Ray-Photoelectron-Spectroscopy Study of Reference Compounds and Thin Oxide Layers.* Physical Review B, 1994. **49**(16): p. 11159-11167.
[42] A. J. Bard, R.P., and J. Jordan, *Standard Potentials in Aqueaus Solutions*. 1985, New York: Marcel Dekker.
[43] Pulver, D., et al., *Thermal oxides of In0.5Ga0.5P and In0.5Al0.5P.* Journal of Vacuum Science & Technology B, 2001. **19**(1): p. 207-214.
[44] Hinkle, C.L., et al., *GaAs interfacial self-cleaning by atomic layer deposition.* Applied Physics Letters, 2008. **92**(7).
[45] Timm, R., et al., *Reduction of native oxides on InAs by atomic layer deposited Al2O3 and HfO2.* Applied Physics Letters, 2010. **97**(13).
[46] Ali, A., et al., *Fermi level unpinning of GaSb (100) using plasma enhanced atomic layer deposition of Al2O3.* Applied Physics Letters, 2010. **97**(14).
[47] Petrovykh, D.Y., et al., *Self-Assembled Monolayers of Alkanethiols on InAs.* Langmuir, 2009. **25**(20): p. 12185-12194.
[48] McGuiness, C.L., et al., *Molecular self-assembly at bare semiconductor surfaces: Investigation of the chemical and electronic properties of the alkanethiolate-GaAs(001) interface.* Journal of Physical Chemistry C, 2007. **111**(11): p. 4226-4234.
[49] Knoben, W., S.H. Brongersma, and M. Crego-Calama, *Preparation and Characterization of Octadecanethiol Self-Assembled Monolayers on Indium Arsenide (100).* Journal of Physical Chemistry C, 2009. **113**(42): p. 18331-18340.
[50] Arthur, J.R., *Molecular beam epitaxy.* Surface Science, 2002. **500**(1-3): p. 189-217.

[51] Joyce, B.A., *Molecular-Beam Epitaxy.* Reports on Progress in Physics, 1985. **48**(12): p. 1637-1697.
[52] Kim, H.S., et al., *Mid-IR focal plane array based on type-II InAs/GaSb strain layer superlattice detector with nBn design.* Applied Physics Letters, 2008. **92**(18).